The Islamic University–Gaza
Research and Postgraduate Affairs
Faculty of Science
Master of Physics

الجامعة الإسلامية – غزة
شئون البحث العلمي والدراسات العليا
كلية العلوم
ماجستير في الفيزياء

Modeling of Newly Multilayer Waveguide Structure Containing Diamond-Like-Carbon, Porous Silicon and Left-Handed Materials

تصميم بنية دليل موجي جديد متعددة الطبقات تحتوي على مادة الكربون شبيه الألماس، السليكون المثقوب والمواد اليسارية

Student Name

Sameh M. A. Al Tanany

Supervised by

Prof. Dr. Mohammed M. Shabat

Professor of Theoretical Physics and Applied Mathematics

A thesis submitted in partial fulfillment
of the requirements for the degree of
Master of Science in Physics

April/2016

إقــــــرار

أنا الموقع أدناه مقدم الرسالة التي تحمل العنوان:

Modeling of Newly Multilayer Waveguide Structure Containing Diamond-Like-Carbon, Porous Silicon and Left-Handed Materials

تصميم بنية دليل موجي جديد متعددة الطبقات تحتوي على مادة الكربون شبيه الألماس، السليكون المثقوب والمواد اليسارية

أقر بأن ما اشتملت عليه هذه الرسالة إنما هو نتاج جهدي الخاص، باستثناء ما تمت الإشارة إليه حيثما ورد، وأن هذه الرسالة ككل أو أي جزء منها لم يقدم من قبل الآخرين لنيل درجة أو لقب علمي أو بحثي لدى أي مؤسسة تعليمية أو بحثية أخرى.

Declaration

I understand the nature of plagiarism, and I am aware of the University’s policy on this.

The work provided in this thesis, unless otherwise referenced, is the researcher's own work, and has not been submitted by others elsewhere for any other degree or qualification.

Student's name: سامح معين عاشور الطناني :اسم الطالب

Signature: :التوقيع

Date: 2016/4/6 :التاريخ

Abstract

Due to their excellent physical properties, former researches on Diamond-like carbon (DLC) and Porous silicon (PS) structures showed good results in the field of photovoltaic devices. In the last two decades, many researchers have reported the exceptional properties of newly synthesized materials that are not found in nature. Those materials are termed as Left-Landed Materials (LHMs).

The aim of this thesis is to study transmitted, reflected and loss powers of a multilayer structure composed of LHM, PS and DLC placed in vacuum when transverse electric plane waves are incident on it. The electromagnetic transmitted, reflected and loss powers as a functions of the incident frequency have been computed numerically and plotted using MATLAB software.

In this thesis, theoretical and analytical investigations of electromagnetic wave propagation through the proposed structure are achieved. A transverse electric polarized plane waves are normally and obliquely incident upon the proposed structure. The reflected, transmitted and loss powers of structure have been studied. For left-handed material, two cases, the loss-less and loss case are considered. In our calculations, we apply the transfer matrix approach. In order to calculate the reflected, transmitted and loss powers, reflection and transmission coefficients have been formulated. In computations, the effect of changing the values of dissipation factor, thicknesses of slabs and angles of incidence has been studied.

In this work, the results show an excellent results for high transmission of the incident waves for certain frequency bands. Hence, the studied structure would be promising to be utilized in the field of solar cells.

Keywords: *Diamond-Like Carbon, Left-handed materials, Porous silicon, Solar Cells, Waveguide***.**

Abstract in Arabic

ملخص البحث

لقد أجريت العديد من البحوث العلمية على مادتي الكربون شبيه الألماس والسيليكون ذو الثقوب وأعطت تلك البحوث نتائجاً ايجابيةً في مجال الأجهزة الكهروضوئية, وتعزى تلك النتائج إلى الخواص الفيزيائية الممتازة لكل من المادتين. في العقدين المنصرمين تم انجاز العديد من الأبحاث لدراسة الخواص الاستثنائية لمواد حديثة التصنيع وغير الموجودة في الطبيعة. تلك المواد تدعى المواد يسارية الجانب.

يركز البحث على دراسة النفاذ والانعكاس للأمواج المستوية الكهربية المستعرضة الساقطة عبر تركيب طبقي موضوع في الفراغ ومكون من كلٍ من المادة اليسارية الجانب الكربون شبيه الألماس, والسيليكون ذو الثقوب. لقد تم حساب قدرات النفاذ, الانعكاس, والفقد عدديا كاقترانات في التردد الساقط وتم رسمها وذلك كله باستخدام برنامج MATLAB.

يتناول هذا البحث دراسة نظرية وتحليلية لاختراق الأمواج الكهرومغناطيسية عبر التركيب المقترح. لقد تمت دراسة قدرات الانعكاس, النفاذ, والفقد عبر التركيب لموجة مستوية وكهربية مستعرضة تسقط بشكل عمودي و حتى مائل. لقد تم الأخذ بعين الاعتبار حالتي الفقد وعدم الفقد للمادة يسارية الجانب. ولاجراء العمليات الحسابية قمنا بتطبيق طريقة مصفوفة النقل. ولحساب قدرات الانعكاس والنفاذ والفقد, تم إيجاد صيغ رياضية لمعاملات الانعكاس والنفاذ. أثناء الحسابات, لقد تمت دراسة تأثير تغيير القيم العددية لكل من معامل الفقد وسمك الطبقة وزاوية السقوط للموجة.

في هذا العمل, تم الحصول على نتائج ممتازة لنفاذ كبير عبر التركيب لموجات ساقطة عليه بترددات معينة الأمر الذي يجعل منه تركيباً واعداً في المستقبل ليتم توظيفه في حقل الخلايا الشمسية.

كلمات مفتاحية: الكربون شبيه الألماس، المواد يسارية, السليكون ذو ثقوب، الخلايا الشمسية، الموجه الموجي.

Dedication

To whom he strives to bless comfort and welfare and never stints what he owns to push me in the success way,, To the big heart my dear father

To the Spring that never stops giving, who weaves my happiness with strings from her merciful heart ,, to my dear mother

To whose love flows in my veins, and my heart always remembers them ,, to my brothers and sisters

To those who reworded to us their knowledge simply and from their thoughts made a lighthouse guides us through the knowledge and success path, To our honored teachers and professors

To my homeland ,, (Palestine) ,, capital city (Jerusalem) ,, city (Gaza)

I guide this research

Sameh M. A. Al Tanany

Acknowledgment

In the name of Allah to whom I am overwhelmed with gratitude for his continuous help and guidance throughout the path of knowledge.

To the utmost knowledge lighthouse, to our greatest and most honored prophet Mohamed - May peace and grace from Allah be upon him. I would like to express my gratitude to all those who gave me the possibility to complete this thesis.

First and foremost I offer my sincerest gratitude to my supervisor Prof. Mohammed M. Shabat for his continuous guidance and direction in this research work. This thesis would not have been possible without him. I express my appreciation to Dr. Abdul-Aziz M. Al-Jalal and Dr. Muin F. Ubeid to be a part of my evaluation committee and for their fruitful suggestions.

My hearty gratitude goes to my father for his innumerable sacrifices and struggles and vast patience to make me reach this stage of qualification and success. My heartfelt thankfulness goes to my mother for her abundant love, care and prayer throughout my life. I express my appreciation to my beloved brothers, and my beloved sisters for their supports and du’aa.

Table of Contents

Declaration II

Abstract III

Abstract in Arabic IV

Dedication V

Acknowledgment VI

Table of Contents VII

Chapter 1 1

Review of Waveguides 1

- 1.1 Waveguide 1
  - 1.1.1 Description of Waveguide 1
  - 1.1.2 Maxwell’s Equations and Field Representation in Waveguides 1
  - 1.1.3 Wave Guiding Modes and Boundary Conditions 4

Chapter 2 7

Diamond-Like Carbon and Porous Silicon 7

- 2.1 Diamond-Like Carbon 7
  - 2.1.1 Definition of Diamond –Like Carbon 7
  - 2.1.2 Properties of Diamond –Like Carbon 9
  - 2.1.3 Dependence of Properties of DLC Films on Deposition Technique and Parameters 10
- 2.2 Porous Silicon 12
  - 2.2.2 Growth Techniques of Porous Silicon 13
  - 2.2.3 Porous Silicon in Solar Cell Processing 15

Chapter 3 17

Left-Handed Material (Theory) 17

- 3.1 Introduction 17
- 3.2 Definition of Left-Handed Materials 18
- 3.3 Backward Propagating Waves in LHM 19
- 3.4 Dielectric Properties of LHMs 20
- 3.5 Poynting Vector and Backward Propagation 23
- 3.6 Phase and Group Velocities in LHMs 27
- 3.7 Negative Sign of the Index of Refraction 27

3.8 Reversal of Snell's law (Negative Refraction Phenomenon) 28
Chapter 4 30
Electromagnetic Wave Propagation in DLC-PS-LHM Waveguide Structure........... 30
4.1 Theory 30
4.2 Numerical Results 40
4.2.1. Negative Refraction of LHMs 42
4.2.2 Effect of the thickness of LHM slab on transmitted, reflected and loss powers of a structure consisting of DLC, PS and LHM 50
4.2.3 Effect of dissipation factor on the transmission of structure consisting of DLC, PS and LHM 53
Chapter 5 56
Effects of Left-Handed Material on New Waveguide Structure for Solar Cell Model 56
5.1 Introduction 56
5.2 Effect of the Angle of Incidence on Wave Propagation 57
5.3 Effect of the Magnetic Permeability of LHM of Incidence on Wave Propagation 59
5.4 Effect of Changing the Thickness on Wave Propagation 62
5.5 Effect of the Composition of the Waveguide Structure on Wave Propagation 66
5.6 Effect of Changing the Value of the Refractive Index of Diamond-Like Carbon and Porous Silicon on Wave Propagation 69
Conclusion 72
References.. 73

List of Figures

Figure(2.1): AFM surface height images of the DLC films deposited at (a) 2 hours, (b) 5 hours and (c) 10 hours.. 8

Figure (2.2): SEM micrograph of deposited surface of a-C:H DLC films. 11

Figure (2.3): SEM image of porous silicon. 13

Figure (2.4): PL spectra of porous silicon prepared by electrochemical etching 14

Figure (3.1): First experimental monodimensionally LHM structures consisted of thin continuous wires and SRRs 18

Figure (3.2): Material parameter space can be conveniently visualized on a set of (ε,μ) axes. Materials which possess a positive permeability are represented by points in the upper half plane. 19

Figure (3.3): Directions of the triads $(E,\ H,\ k)$ and (E,H,S) for ; (a) RHM $(\varepsilon,\mu > \mathbf{0})$. (b) LHM $(\varepsilon,\mu < 0)$. 26

Figure (3.4): Refraction of an incident electromagnetic wave at the interface between two media. (a) Case of two media of the same handedness (either RHMs or LHMs). (b) Case of two media (one of Right-handedness and the other of Left-handedness). 29

Figure (4.1): TE-Wave propagation through a structure consisting of three slabs inserted in vacuum. 31

Figure (4.2): Oblique incidence of electromagnetic wave on DLC,PS and LHM structure embedded in vacuum. 41

Figure (4.3): Calculated LHM permittivity and permeability versus frequency (9 GHz -12 GHz). 42

Figur(4.4): Transmitted, reflected powers and their total sum against frequency (10.3 - 11.5 GHz) for $\theta = 0^\circ$. ($d_{\mathrm{DLC}} = d_{\mathrm{PS}} = d_{\mathrm{LHM}} = 10$ mm, $n_{\mathrm{DLC}} = 1.6$, $n_{\mathrm{PS}} = 2.9$, $\gamma = 0.0$ GHz). 43

Figure (4.5): Transmitted and reflected powers against frequency (10.3 –10.32 GHz) for different angles of incidence ($\theta = 0^\circ$and $\theta = 30^\circ$). ($d_{\mathrm{DLC}} = d_{\mathrm{PS}} = d_{\mathrm{LHM}} = 13.64$ mm, $n_{\mathrm{DLC}} = 2.7$, $n_{\mathrm{PS}} = 1.25$, $\gamma = 0.0$ GHz). 44

Figure (4.6): Transmitted &reflected powers against frequency (10.4- 11.8 GHz) for angle of incidence ($\theta = 30^\circ$) for different structures (DLC/PS/LHM) tri-layer and LHM single layer). The data used are:($d_{\mathrm{DLC}} = d_{\mathrm{PS}} = d_{\mathrm{LHM}} = 13.64$ mm, $n_{\mathrm{DLC}} = 2.7$, $n_{\mathrm{PS}} = 1.25$, $\gamma = 0.0$ GHz). 45

Figure (4.7): Transmitted and reflected powers against frequency (10.4- 11.8 GHz) for different angles of incidence ($\theta = 0^\circ$, $\theta = 30^\circ$, $\theta = 60^\circ$). ($d_{\mathrm{DLC}} = d_{\mathrm{PS}} = d_{\mathrm{LHM}} = 6.82$ mm, $n_{\mathrm{DLC}} = 2.7$, $n_{\mathrm{PS}} = 3$, $\gamma = 0.0$ GHz). 46

Figure (4.8): Transmitted, reflected and loss powers as a function of frequency (10.4-11.8 GHz) for various angles of incidence ($\theta=0^\circ$) for different structures (DLC/PS/LHM) tri-layer and LHM single layer). ($d_{DLC} = d_{PS} = 1$ mm, $d_{LHM} = 5$ mm, $n_{DLC} = 1.6$, $n_{PS} = 2.9$, $\gamma = 0.2$ GHz). 48

Figure (4.9): Transmitted, reflected and powers against frequency (10.4- 11.8 GHz) for normal incidence ($\theta = 0^\circ$) for different structures ((DLC/PS/LHM) tri-layer and LHM single layer). The data used are :($d_{DLC} = d_{PS} = d_{LHM} = 13.64$ mm, $n_{DLC} = 2.7$, $n_{PS} = 3$, $\gamma = 0.2$ GHz). 49

Figure (4.10): Transmitted, reflectted and loss power as a function of frequency (10.4-11.8GHz) for various thicknesses of LHM slab: (d_{LHM}= 0/20/40/60/100 mm). ($d_{DLC} = 85$ nm, $d_{PS} = 30$ nm, $n_{DLC} = 1.6$ $n_{PS} = 2.9$, $\gamma = 0.2$ GHz). 51

Figure (4.11): Transmitted, reflected and loss Power against frequency (9-12 GHz) for two different values of equal thicknesses of DLC, PS and LHM slabs(d =6.82mm, d =13.64 mm). ($n_{DLC} = 1.6$, $n_{PS} = 2.8$, $\theta = 30^\circ$, $\gamma = 0.2$ GHz). 52

Figure (4.12): Transmitted, reflected and loss Power as a function of frequency (9-12 GHz) under the effect of various dissipation factors (γ =0.0, 0.1 and 0.2GHz). ($d_{DLC} = 85$ nm, $d_{PS} = 30$ nm, $d_{LHM} = 30$ mm, $n_{DLC} = 1.6$, $n_{PS} = 2.8$, $\theta = 45^\circ$). 54

Figure (4.13): Transmitted, reflected and loss Power against frequency (9-12 GHz) under the effect of various dissipation factors (γ =0.0, 0.1and 0.2 GHz). ($d_{DLC} = d_{PS} = d_{LHM} = 6.82$ mm, $n_{DLC} = 1.6$, $n_{PS} = 2.8$, $\theta = 30^\circ$). 55

Figure (5.1): Oblique incidence of electromagnetic wave on DLC,PS and LHM structure embedded in vacuum. 57

Figure (5.2): Transmitted and reflected powers as afunction of wavelength (400-1200 nm) for various angles of incidence($\theta = 0^\circ$,$\theta = 30^\circ$,$\theta = 45^\circ$,$\theta = 60^\circ$and $\theta = 89^\circ$). ($d_{DLC} = 85$ nm, $d_{PS} = 30$ nm , $d_{LHM} = 400$ nm, $n_{LHM} = -2$,$\mu_{LHM} = -8$, $n_{DLC} = 1.6$, $n_{PS} = 2.9$). 58

Figure (5.3): Transmitted and reflected powers as afunction of wavelength (400-1200 nm) for various angles of incidence($\theta = 0^\circ$,$\theta = 30^\circ$,$\theta = 45^\circ$,$\theta = 60^\circ$and $\theta = 89^\circ$). ($d_{DLC} = 85$ nm, $d_{PS} = 30$ nm , $d_{LHM} = 200$ nm, $n_{LHM} = -2$ $\mu_{LHM} = -8$, $n_{DLC} = 1.6$, $n_{PS} = 2.9$). 59

Figure (5.4): Transmitted and reflected powers as afunction of wavelength (400-1200 nm) for different values of magnetic permeability of LHM (μ_{LHM} =-4,-5,-6 and -8). ($d_{DLC} = 85$ nm, $d_{PS} = 30$ nm , $d_{LHM} = 200$ nm, $n_{LHM} = -2$, $n_{DLC} = 1.6$, $n_{PS} = 2.9$, $\theta=0^\circ$). 60

Figure (5.5): Transmitted and reflected powers as afunction of wavelength (400-1200 nm) for different values of magnetic permeability of LHM (μ_{LHM} =-4,-5,-6 and -8). ($d_{DLC} = 85$ nm, $d_{PS} = 30$ nm , $d_{LHM} = 400$ nm, $n_{LHM} = -2$, $n_{DLC} = 2.7$, $n_{PS} = 3$, $\theta = 45^\circ$). 61

.... 62

Figure (5.6): Transmitted and reflected powers as afunction of wavelength (400-1200 nm) for different values of magnetic permeability of LHM (μ_{LHM} =-4,-5,-6 and -8). (d_{DLC} = 85 nm, d_{PS} = 30 nm , d_{LHM} =200 nm, n_{LHM}= -2, n_{DLC} =2.7, n_{PS} =3, θ = 45˚)... 62

Figure (5.7): Transmitted and reflected powers as afunction of wavelength (400-1200 nm) for different thicknesses of LHM: d_{LHM} =100, 200 and 400 nm. (d_{DLC} = 85 nm, d_{PS} = 30 nm , n_{LHM}= -2, μ_{LHM} =-4, n_{DLC} =2.7, n_{PS} =3, θ = 60˚)......................... 63

Figure (5.8): Transmitted and reflected powers as a function of wavelength (400-1200 nm) for two different thicknesses of LHM: d_{LHM} =200 nm and d_{LHM} =400 nm. (d_{DLC} = 85 nm, d_{PS} = 30 nm , n_{LHM}= -2, μ_{LHM} =-4, n_{DLC} =1.6, n_{PS} =2.9, θ = 0˚). 64

Figure (5.9): Transmitted and reflected powers as afunction of wavelength (400-1200 nm) under the effect of changing the refractive idecies and thicknesses of DLC and PS. (d_{DLC} = 85 nm/86.9 nm, d_{PS} = 30 nm/47.9 nm, d_{LHM} =200 nm, n_{LHM}= -2, μ_{LHM} =-4, n_{DLC} =1.6, n_{PS} =2.8, θ = 0˚)... 65

Figure (5.10): Transmitted and reflected powers as afunction of wavelength (400-1200 nm) for various thicknesses of LHM: (d_{LHM} =0, 200, 300, 400 and 500 nm). (d_{DLC} = 85 nm, d_{PS} = 30 nm , n_{LHM}= -2, μ_{LHM} =-4, n_{DLC} =1.6, n_{PS} =2.9, θ = 0˚). 66

Figure (5.11): Transmitted and reflected powers as afunction of wavelength (400-1200 nm) for different types of structure (DLC/PS double layer, LHM single layer and DLC/PS/LHM trilayer). (d_{DLC} = 85.9 nm, d_{PS} = 47.9 nm , d_{LHM} =200 nm, n_{LHM}= -2, μ_{LHM} =-4, n_{DLC} =2.7, n_{PS} =1.25, θ = 0˚)... 67

Figure (5.12): Transmitted and reflected powers as afunction of wavelength (400-1200 nm) for different types of structure (DLC/PS double layer, LHM single layer and DLC/PS/LHM trilayer). (d_{DLC} = 85 nm, d_{PS} = 30 nm , d_{LHM} =200 nm, n_{LHM}= -2, μ_{LHM} =-4, n_{DLC} =2.7, n_{PS} =1.25, θ = 0˚).. 68

Figure (5.13): Transmitted and reflected powers as afunction of wavelength (400-1200 nm) for different types of structure (DLC/PS double layer, LHM single layer and DLC/PS/LHM trilayer). (d_{DLC} = 85 nm, d_{PS} = 30 nm , d_{LHM} =400 nm, n_{LHM}= -2, μ_{LHM} =-4, n_{DLC} =1.6, n_{PS} =1.25, θ = 30˚)... 69

Figure (5.14): Transmitted and reflected powers as afunction of wavelength (400-1200 nm) for different values of refractive indcies of DLC and PS: (d_{DLC} = 85 nm, d_{PS} = 30 nm , d_{LHM} =200 nm, n_{LHM}= -2, μ_{LHM} =-4, θ = 0˚)....................................... 70

Figure (5.15): Transmitted and reflected powers as afunction of wavelength (400-1200 nm) for different values of refractive indcies of DLC and PS: (d_{DLC} = 85 nm, d_{PS} = 30 nm , d_{LHM} =200 nm, n_{LHM}= -2, μ_{LHM} =-4, θ = 60˚)..................................... 71

Chapter 1

Review of Waveguides

In this chapter, we establish the fundamental concepts of electromagnetic wave guidance in waveguiding structures. Section 1.1 describes the nature of waveguides. Section 1.1.1 analyzes the guided electromagnetic fields using Maxwell’s equations and Helmholtz wave equation. Section 1.1.2 illustrates the modes of waveguides and the boundary conditions are imposed in our studies.

1.1 Waveguide

1.1.1 Description of Waveguide

Consider a wave propagation through a hollow metallic cylinder. If the cylinder has no end surfaces then it is called a waveguide. Waveguide is used to transfer electromagnetic power efficiently from one point to another.

In general, waveguides possess cylindrical shape and have an arbitrary cross section that is generated by a straight line moving parallel to the transmission direction characterized by certain unit vector.

1.1.2 Maxwell’s Equations and Field Representation in Waveguides

For simplicity, consider the shape and the cross-sectional size of waveguide structures are constants along the waveguide axis. Assuming that the waveguide is filled with a uniform medium having both real permittivity ε and permeability μ (i.e., non-dissipative), then the guided electric and magnetic fields inside the waveguide obey Maxwell's equations that takes the form(Kawano & Kitoh, 2004; Okamoto, 2010):

$$\vec{\nabla}.\vec{E} = 0, \qquad 1.1$$

$$\vec{\nabla}.\vec{B} = 0, \qquad 1.2$$

$$\vec{\nabla} \times \vec{E} = i\omega\overrightarrow{B,} \qquad 1.3$$

$$\vec{\nabla} \times \vec{B} = -i\omega\mu\varepsilon\vec{E}. \qquad 1.4$$

Where $\vec{E}, \vec{B}$ and $\omega$the electric field intensity, the magnetic flux density and angular frequency respectively. a harmonic sinusoidal time dependence $e^{-i\omega t}$ is assumed.

Consequently, both E and B satisfy the form of a three dimensional Helmholtz wave equation

$$[\nabla^2 + \mu\varepsilon\omega^2]\begin{pmatrix} E \\ B \end{pmatrix} = 0, \qquad 1.5$$

Where the Laplacian ∇^2 is given by:

$$\nabla^2 = \frac{\partial^2}{\partial x^2} + \frac{\partial^2}{\partial y^2} + \frac{\partial^2}{\partial z^2}, \qquad 1.6$$

For a wave travels in a certain direction, say the z direction, the wave number may be real or complex and the wave equation reduces to the two dimensional form

$$\left[{\nabla_t}^2 + (\mu\varepsilon\omega^2 - k^2)\right]\begin{pmatrix} E \\ B \end{pmatrix} = 0, \qquad 1.7$$

${\nabla_t}^2$ is the transverse part of the laplacian operator and given by

$${\nabla_t}^2 = \nabla^2 - \frac{\partial^2}{\partial z^2}. \qquad 1.8$$

Where the gradient operator transverse to z-axis is $\overrightarrow{\nabla_t} = \vec{\nabla} - \frac{\partial}{\partial z}\hat{z}$.

$\frac{\partial}{\partial z}\hat{z} = ik\hat{k}$; $\hat{k}$ is a unit vector of wave propagation. Hence, $\frac{\partial^2}{\partial z^2} = -k^2$.

Now, the electromagnetic fields are separated into two components, component parallel to the *z* axis and component transverse to the *z* axis

$$\vec{E} = \vec{E}_z + \vec{E}_t, \tag{1.9}$$

where

$$\vec{E}_z = E_z\hat{z}\,, \tag{1.10}$$

$$\vec{E}_t = (\hat{z} \times E) \times \hat{z}\,. \tag{1.11}$$

$\hat{z}$ is a unit vector in the z direction.

In analogy, for a magnetic field B we have

$$\vec{B} = \vec{B}_z + \vec{B}_t\,, \tag{1.12}$$

where

$$\vec{B}_z = B_z\hat{z}\,, \tag{1.13}$$

$$\vec{B}_t = (\hat{z} \times B) \times \hat{z}. \tag{1.14}$$

Maxwell's equations (1.1-1.4) can be rewritten in terms of parallel and transverse components as

$$\hat{z} \cdot \left(\vec{\nabla}_t \times \vec{E}_t\right) = i\omega B_z, \tag{1.15}$$

$$\frac{\partial \vec{E}_t}{\partial z} + i\omega\hat{z} \times \vec{B}_t = \vec{\nabla}_t E_z, \tag{1.16}$$

$$\hat{z} \cdot \left(\vec{\nabla}_t \times \vec{B}_t\right) = -i\omega\mu\varepsilon E_z, \tag{1.17}$$

$$\frac{\partial \vec{B}_t}{\partial z} - i\omega\mu\varepsilon\hat{z} \times \vec{E}_t = \vec{\nabla}_t B_z\,, \tag{1.18}$$

$$\vec{\nabla}_t \cdot \vec{B}_t = -\frac{\partial B_z}{\partial z}, \qquad 1.19$$

$$\vec{\nabla}_t \cdot \vec{E}_t = -\frac{\partial E_z}{\partial z}. \qquad 1.20$$

It is seen from the equations in (1.16) and (1.18) that if E_z and B_z are known the transverse components of E and B are determined.

For the non-vanishing of at least one of E_z and B_z, the transverse electric and magnetic fields components takes the forms:

$$\vec{E}_t = \frac{i}{\mu\varepsilon\omega^2 - k^2}\left[k\vec{\nabla}_t E_z - \omega\hat{z} \times \vec{\nabla}_t B_z\right], \qquad 1.21$$

and

$$\vec{B}_t = \frac{i}{\mu\varepsilon\omega^2 - k^2}\left[k\vec{\nabla}_t B_z + \mu\varepsilon\omega\hat{z} \times \vec{\nabla}_t E_z\right]. \qquad 1.22$$

Where the wave propagation in the positive z direction is assumed. For a wave propagate in the negative z direction, change the sign of the wave vector k.

1.1.3 Wave Guiding Modes and Boundary Conditions

From equations (1.15) to (1.20) it is seen that if $E_z = 0$ and $B_z = 0$, then this requires that $E_t = E_{TEM}$ satisfies

$$\vec{\nabla}_t \times \vec{E}_{TEM} = 0 \qquad 1.23$$

and

$$\vec{\nabla}_t \cdot \vec{E}_{TEM} = 0 \qquad 1.24$$

This means the E_{TEM} is a solution of an electrostatic problem in two dimensions.

Where the designation TEM refers to a special type of solutions, called the transverse electromagnetic wave. This TEM solution possesses only electromagnetic field components transverse to the direction of wave propagation. A property of TEM mode which is of great interest is the absence of a cutoff frequency. The cut off frequency acts as a switch between the propagating and evanescent wave modes frequencies.

For waves propagation as $e^{\pm ikz}$, the magnetic field according to equation (1.18) is

$$\vec{B}_{TEM} = \pm\sqrt{\mu\varepsilon}\hat{z} \times \vec{E}_{TEM} \qquad 1.25$$

The axial wave number k as can be seen from equation(1.7) is given by

$$k = \omega\sqrt{\mu\varepsilon} \qquad 1.26$$

For a given frequency ω, only certain values (modes) of wave number K can occur.

At the surface of a TEM mode waveguide, the boundary conditions on E_z is

$$E_z\big|_s = 0 \qquad 1.27$$

Let n stands for a unit vector normal at the surface of a waveguide. From the component of equation (1.18) parallel to n it can be inferred that the corresponding boundary condition on B_z is

$$\left.\frac{\partial B_z}{\partial n}\right|_s = 0 \qquad 1.28$$

Where $\partial/\partial n$ is the normal derivative at a point on the waveguide surface.

The boundary conditions on the magnetic and electric fields are different. Thus, the waves are divided into two distinct classes:

First Class: Transverse Electric Waves (TE)

For this class, the only wave components that can exist for a waveguide are the transverse field components E_t $i.e.$, $E_z = E_z(x, y) = 0$ everywhere ; boundary condition , $\left.\frac{\partial B_z}{\partial n}\right|_s = 0$.

Second Class: Transverse Magnetic Waves (TM)

For this class, there is no component of the magnetic field parallel to the direction of electromagnetic waves *i.e.*, $B_z = B_z(x,y) = 0$ everywhere; the boundary condition $E_z\big|_s = 0$. For a specified axial component of the wave fields the designations "magnetic or H waves " and " electric or E waves " are sometimes used instead of TE and TM waves, respectively.

Chapter 2

Diamond-Like Carbon and Porous Silicon

In this chapter, we used the materials, Diamond-Like Carbon (DLC), and Porous silicon (PS), and Left-Handed Materials(LHM) for solar cells application. These materials are presented in some details in chapter 2 and chapter 3.

In section 2.1, diamond-like carbon films, as one of a peculiar wave-guiding structures that are utilized for solar cells applications, will be introduced. In Section 2.1.1, diamond-like carbon has been defined. In Section 2.1.2,a remarkable properties of DLC which enhances its utilization in many industrial applications including solar cells, has been highlighted. In section 2.1.3, the effect of the deposition technical parameters on the resultant tribological properties of the DLC films, has been discussed. In section 2.1.4, the usage of the DLC films in many industrial applications and manufacturing purposes, has been exhibited. In section 2.2, porous silicon has been introduced. In section 2.2.1, PS structure and its interesting properties for the solar cell applications, has been discussed. In section 2.2.2, some of the growth techniques of the PS passivation on solar cells, has been mentioned. In section 2.2.3, the utilization of PS in solar cell processing, has been demonstrated.

2.1 Diamond-Like Carbon

2.1.1 Definition of Diamond –Like Carbon

DLC is an amorphous type of carbon possessing cross-linked lattice of trigonal sp^2- and tetragonal sp^3-hybridized carbon atoms with relatively large ratio of sp^3/sp^2 carbon content (Butt, Khaleeq-ur-Rahman, Ali, Akmal, & Naseem, 2015; Masuko, Ono, Aoki, Suzuki, & Ito, 2015; Okubo, Tsuboi, & Sasaki, 2015). The sp^3 bonding of DLC causes flawless regularity of the carbon fabric, that offers advantageous properties like substantial hardness, chemical and electrochemical inertness, optical pellucidity, remarkable heat conductivity, large electrical resistivity, and small wear rate in different tribological systems (Sharma, Barhai, & Kumari, 2008; Vetter, 2014). In figure 2.1, AFM images of DLC films deposited at different deposition times are shown. DLC films are apt for optoelectronic use with its wide (0.0 eV–5.5 eV) and variable band gap, which is adjusted by altering the sp^2 and sp^3 of manganese bonding ratio (Ikeyama & Sonoda, 2013). Doping with nitrogen is a possible technique to alter the sp^2 and sp^3 bonded carbon ratios and consequently regulate the properties of the DLC films (Seker, Ozdamar, Esen, Esen, & Kavak, 2014). The smaller the sp2/sp3 ratio, the larger the optical band gap (Ramachandran, Tao et al. 2006). By changing the growth parameters, it is possible to change the refractive index of the DLC films from 1.6 to 2.7 (Klyui, Litovchenko et al. 2002).

DLC films are appropriate substances since they are advantageous to raise the transmittance or lower the undesirable surface reflections (Chen, Yang, Song, Yu, & Qian, 2013).

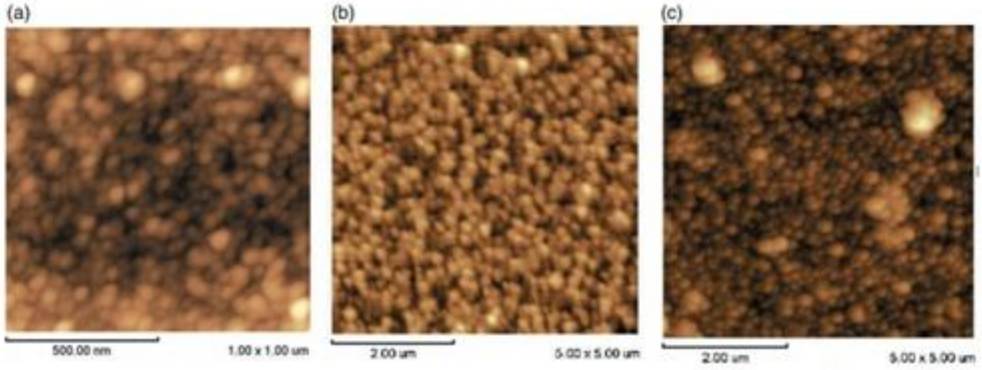

Figure(2.1): AFM surface height images of the DLC films deposited at (a) 2 hours, (b) 5 hours and (c) 10 hours.(This figure is in the electronic version) (Yan, Xu, Yang, Liu, & Xue, 2004).

2.1.2 Properties of Diamond –Like Carbon

Diamond-like carbon (DLC) films have been thoroughly studied and extensively deployed for over 20 years decades owing to its sublime characteristics(Yang, et al., 2015) .The structural properties of the DLC film were scrutinized with Raman spectroscopy (Ramachandran, et al., 2006). It was discovered that DLC possesses comparable optical, electrical, chemical and mechanical properties as diamond (Seker, et al., 2014). Nevertheless, the color of DLC is quite often dark brown or black, and with the exception of some DLC coverings for tools, their color are rainbow-like. The rainbow color is a feature of nearly hydrogen free DLC coverings which are coated by sputtering and pulsed laser ablation (Ikeyama & Sonoda, 2013).

It is widely-familiar that amorphous carbon-based coatings (DLC) offers magnificent mechanical and tribological features like high hardness, high elastic modulus, low friction and low wear, chemical and radiation solidity along with a likelihood to alter their optical properties by changing the deposition variables(Kalin, Kogovšek, & Remškar, 2013; Litovchenko & Klyui, 2001; Vitu, Escudeiro, Polcar, & Cavaleiro, 2014). The latter allows multi-layer coatings to develop which satisfy the requisites of ideal antireflection and protection of SCs at the same time (Litovchenko & Klyui, 2001). Nonetheless, large inner compressive stress in DLC films owing to substantial sp^3 bonding and inadequate adherence of DLC films with the majority of substrates because of substantial incongruity in their thermal expansion coefficient hinders their real-life deployment greatly. To surmount these disadvantages one can assimilate different metals in DLC films, which both lowers internal compressive stress as well as improves adherence to substrate. Furthermore, other mechanical, optical, electrical, chemical, and magnetic properties of DLC films are altered(Butt, et al., 2015).

Doped or alloyed DLC coatings usually display enhanced tribological features both by reducing the friction and wear and also by the stabilization of the tribological features in various testing conditions (Vitu, et al., 2014). Altered by changing the degree of nitrogen assimilation during film deposition, several benefits such as low background current, large potential window and chemical inactivity in chemically aggressive conditions are provided by nitrogen doped DLC (DLC:N)(Seker, et al., 2014).

The tribological features of untainted DLC layers are largely contingent on their physical construction and testing environmental surroundings (Vitu, et al., 2014). Nonetheless, deeper understanding of their tribological features is needed to lower frictional dissipation and so lower energy usage in the car industry (Mutafov, Lanigan, Neville, Cavaleiro, & Polcar, 2014).

The hardness and the elastic features tests of the DLC layers have been confirmed by the Nano-indentation tests using a MTS XP Nano Indenter under an uninterrupted stiffness measurement mode and furnished with a Berkovich indenter (Staia, Cabrera et al. 2015).

Boundary-lubrication circumstances offer the most heavily loaded contacts in tribological uses that predetermine the behavior and outcome of many sophisticated engineering systems (Tasdemir, 2014). In the quest for the optimal surface solutions under such circumstances, DLC is broadly-used as surface layering material owing to its intrinsic and excellent features like high physical hardness, low friction coefficient, chemical inertness, high wear resistance and high biocompatibility (Kalin, et al., 2013; Seker, et al., 2014).

2.1.3 Dependence of Properties of DLC Films on Deposition Technique and Parameters

It is feasible to regulate the mechanical features of DLC films with deposition processes, and it is common knowledge that these physical properties are contingent upon the amount of hydrogen in the DLC films(Okubo, et al., 2015). In brief, the DLC layers coated on temperature sensitive substrates, like steel, can be classified into 2 major categories — hydrogenated films deposited either by plasma enhanced chemical vapor deposition (PECVD) or by reactive magnetron sputtering (a-C:H) and non-hydrogenated films prepared by non-reactive magnetron sputtering (a-C).

Non-hydrogenated coatings typically do better in humid conditions, while hydrogenated coatings are remarkable in dry sliding and inert gas conditions approaching friction values in the range of 0.001–0.2 (Vitu, et al., 2014).

There are few methods to deposit diamond like carbon films (Seker, et al., 2014). DLC films can be deposited by numerous processes, e.g. enhanced deposition, ion beam deposition, ion assisted sputtering, sputtering, cathodic arc evaporation, plasma assisted chemical vapor (PACVD) deposition, plasma based ion implantation, pulsed laser deposition and electron cyclotron resonance (ECR) plasma (PBII & D) and so on (Hatada, Flege, Bobrich, Ensinger, & Baba, 2014; Kalin, et al., 2013; Seker, et al., 2014). The utilization of electron cyclotron resonance (ECR) plasma enhanced deposition has numerous benefits such as lowering Hydrocarbon impurities at low deposition pressures along with the capability to work at low temperatures and thus to utilize elastic substrates like polyamide(Seker, et al., 2014). DLC films with thicknesses ranging from 100 nm up to 1 μm were coated onto 0.5 mm thick Si and quartz wafers by PECVD (Ramachandran, et al., 2006). The DLC film, known formally as LRSO -TM (hydrogenated a-C:H), was deposited by Teer Coatings (see figure 2.3) , U.K., by means of closed field unbalanced magnetron sputtering ion platting (CFUBMSIP), coupled with plasma assisted chemical vapor deposition (PACVD)(Staia, et al., 2015).

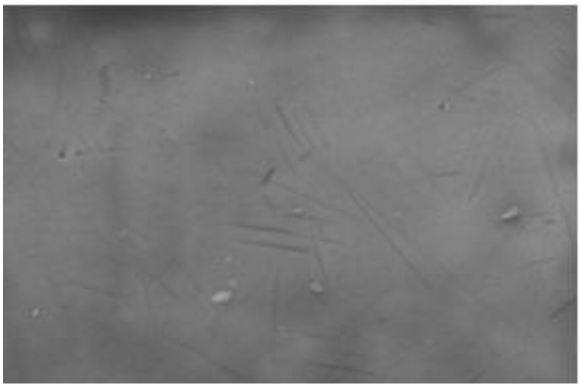

Figure (2.2): SEM micrograph of deposited surface of a-C:H DLC films (Mobarak & Chowdhury, 2014).

2.2 Porous Silicon

2.2.1 Introduction to Porous silicon

Porous silicon (PS) is a nanoengineered substance which exhibits unique optoelectronic behavior due to having the potential to be utilized in the antireflective layers of photovoltaic cells owing to its smaller reflectivity and passivating properties (González-Díaz, Guerrero-Lemus, Borchert, Hernández-Rodríguez, & Martínez-Duart, 2007; Vitanov, Goranova, Stavrov, Ivanov, & Singh, 2009). PS aids in boosting the efficacy of optoelectronic devices by enhancing light capturing in the active zone due to its surface morphology which constitutes an irregular web of minute pores entering Si (Salman, Omar, & Hassan, 2012). Because of its porous nature, the PS refractive index depends on the porosity and can vary from 1.25 to 3 (Bisi, Ossicini et al. 2000).

It has been demonstrated that the development of a permeable layer under ideal technical conditions yields substantial enhancement in the key benchmark figures that typically characterize PV cells-short-circuit current and open-circuit voltage (Adamian, Hakhoyan, Aroutiounian, Barseghian, & Touryan, 2000).

Porous silicon has evolved to become an integral component of solar cells owing to its efficacious anti-reflecting coating (ARC) along with other properties such as a widened band gap, a roughened surface, wide absorption bandwidth and wide transmission in the optical window (700–1000 nm) (Ramizy, Aziz, Hassan, Omar, & Ibrahim, 2011; Ramizy, Hassan, Omar, Al-Douri, & Mahdi, 2011; Salman, et al., 2012). In figure 2.3, SEM image of PS is shown. A critical factor that accounts for the utilization of PS is the raised short circuit current values which arises from the reduced recombination speed at the surface. This benefit occurs to the passivating behavior of PS. The velocity of recombination is approximately 105–106 cm/s at the fore end of a nonpassivated silicon surface but falls to a mere 10^2–10^3cm/s for its passivated counterpart (Vitanov, Delibasheva, Goranova, & Peneva, 2000). First application of PS as an ARC for solar cells was made almost 15 years ago and since that time different research groups have tested PS material for photovoltaic devices (RR Bilyalov, et al., 2000).

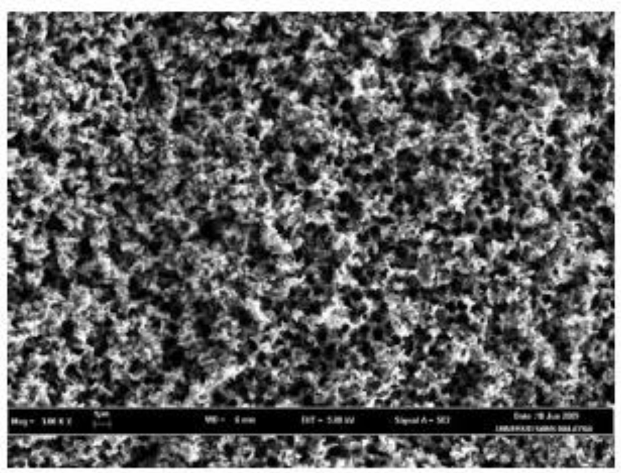

Figure (2.3): SEM image of porous silicon (Aziz, Ramizy, Ibrahim, Hassan, & Omar, 2011).

2.2.2 Growth Techniques of Porous Silicon

Both chemical and electrochemical techniques are used for growing PS ARC on multi- and mono-Silicon solar cells. For multi-Si PV cells an efficiency of 10.4% for large area (10×10 cm^2) multicrystalline silicon (mc-Si) solar cell with screen-printed contacts is derived using a polymeric film for safety from impact. For the electrochemical procedure for PS ARC fabrication an 11.5% efficiency is obtained without further ARC deposition for the mc-Si cells with the same area and contacts (RR Bilyalov, et al., 2000). In figure 2.4, PL spectra for PS fabricated by electrochemical etching is shown.

Nonetheless electrochemical etching procedures are accepted as being aggressive, so to take advantage from PS as an ARC or as a passivating layer, very brief anodization duration (<5 s) must be used to prevent ruining the junction and damaging the front grid contacts (Saadoun, Ezzaouia, Bessaıs, Boujmil, & Bennaceur, 1999).

Brendel has performed electrochemical etching of porous Si layer into the substrate based on homoepitaxial growth of monocrystalline Si films and yielded a module efficiency of 10% (Ramizy, Hassan, et al., 2011).

An efficacy of 13.2% has been attained on a 25 cm^2 multicrystalline silicon (mc-Si) PV cell by utilizing the electrochemical procedure while efficiencies ranging from 12% to 13% are have been attained for very huge (100–164 cm^2) commercial mc-Si cells with a PS emitter formed by chemical technique(RR Bilyalov, et al., 2000).

Lately, promising outcomes have been obtained by Schirone et al., who fabricated enormous-area solar cells by transforming the exterior Si layer into PS by etching in controlled solutions; they observed that a 100 cm^2 cell which boasted an efficiency of 10.4% (AM1.5), possessed an improved photon absorption at near-IR, coupled with improved surface passivation (Saadoun, et al., 1999).

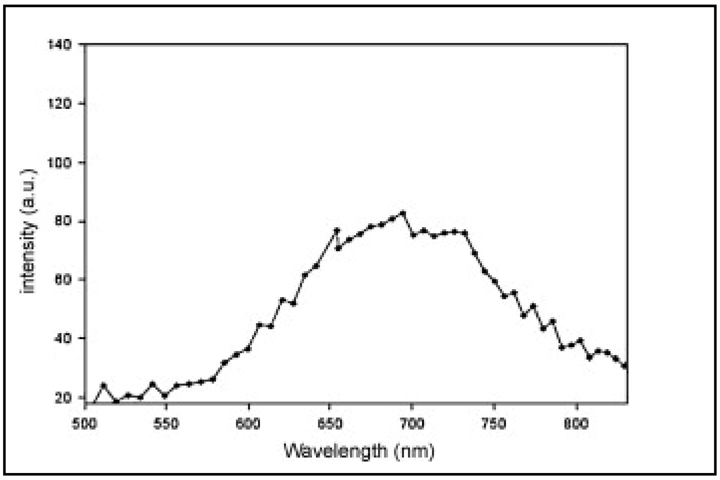

Figure (2.4): PL spectra of porous silicon prepared by electrochemical etching (Aziz, et al., 2011).

Porous silicon wafers were made using the vapor etching (VE) procedure, which involves exposing Si substrates to acidic fumes exuding from a concoction of HNO_3 (65%) and HF (40%) (Aouida, Saadoun, Boujmil, Rabha, & Bessaıs, 2004).

Chemical Vapor Etching (CVE) technique was used to perform front PS layer (RR Bilyalov, et al., 2000). Morphological investigation explicitly demonstrates that a Si coating with epitaxial quality can be deposited by CVD on dual ($\frac{20}{60}$%) PS which maintains the integrity of its permeable structure, even though a reduction in permeability arising from pore filling was noticed (Renat Bilyalov, et al., 2001). Alternatively, PS can be made by anodic dissolution of silicon in a chemical concoction of HF and ethanol or acetic acid (Renat Bilyalov, et al., 2001).

2.2.3 Porous Silicon in Solar Cell Processing

The extent of surface reflection is the main hindrance in efficacious solar cell (Ramizy, Hassan, et al., 2011). Surface texturization lowers the photon reflectivity and thus raises the photon-capturing over a broader wavelength window. The PS displayed remarkable photon- capturing at wavelengths ranging from 400 to 1000 nm (Salman, et al., 2012).

The primary performance-enhancing variable for PS is the large extent of surface irregularity and reduced net refractive index in contrast with c-Si, which can lower the reflection losses of the solar flux (Salman, et al., 2012).

Solar cells made PS ARC accompanied by the presence of nanocrystal coating demonstrated that the conversion ratio rose by 14.5% compared with the unetched sample (Ramizy, Aziz, et al., 2011).

The smallest net reflectance of the PS layers was acquired at 20 min etching duration and portrayed excellent photon- capturing. Therefore, high efficiency of solar cell of 18.15% was acquired with PS ARC coating at 20 min etching duration (Salman, et al., 2012).

PS can be incorporated with other structures to raise the conversion efficiency of the photovoltaic cells. For instance, for mc-Si solar cells the conversion efficiency (η) rose from 7% (for a typical untreated cell) to an impressive 11.8% subsequent to attaining BMCs-PS integration), the open-circuit voltage (Voc) rose slightly from 0.55 to 0.56 V after which an improvement of the current collection and lessening of the surface recombination via the PS layer occurred. Hence, the reflectivity fell to 8% in the 450–950 nm wavelength window and the net minority carrier diffusion distance rose from 75 to 110 μm (Rabha & Bessaïs, 2010). The optimization of a PS selective emitter formation leads to a 14.1% efficiency mc-Si cell made without texturization, surface passivation or further ARC deposition (RR Bilyalov, et al., 2000). Numerous investigations demonstrated that the properties of monocrystalline silicon PV cells can be enhanced by coating the n^+ emitter area with permeable silicon layer (PLS). An improvement from 20% to 50% in short-circuit current (Isc) was seen, which can be justified by invoking the unique electrical and optical properties of PSL (Vitanov, et al., 2000).

Chapter 3

Left-Handed Material (Theory)

3.1 Introduction

The concept of left-handed materials (LHMs) (sometimes termed as Metamaterial (MMs) was introduced by Veselago theoretically nearly four decades ago. The interesting and unusual physical properties, such as a reversed Doppler shift, a reversed Snell refraction (negative refraction) and a backward Cerenkov radiation were described by Veselago (M. Ubeid, M. Shabat, & M. Sid-Ahmed, 2013; Soukoulis, Kafesaki, & Economou, 2006; Veselago, Braginsky, Shklover, & Hafner, 2006; Zhang, 2004).

A realization of the artificial periodic continuous wires (CWs) is presented by Pendry and his group in 1996 which shows negative permittivity and in 1999 of the split-rings which shows negative permeability (Pasakawee, 2012; Pendry, Holden, Robbins, & Stewart, 1999).

Magnetized ferrite is an additional alternative to SRR to provide negative permeability (M. Ubeid, M. Shabat, & M. Sid-Ahmed, 2012; M. F. Ubeid, M. M. Shabat, & M. O. Sid-Ahmed, 2012). Hence, a LHM (negative refraction material) can be formed by inserting a periodic continuous wires into the ferrite material. An Experimental realization of negative index of refraction was achieved. In 2001, D. R. Smith et al. fabricated a left-handed sample by periodically arranging metallic printed lines(or rods) that exhibit a negative permittivity and split-ring resonators (SRR) that exhibit a negative permeability into an arrays, and for the first time verified the real existence of left-handed material by observing a “negative” refraction of a microwave frequency beam transmitted through a prism-shaped sample (Ran, Huang-Fu et al. 2005). Many experimental measurements on LHMs are performed on microwave frequency region. However, there is a tendency to increase the operation frequency up to terahertz and even optical frequencies.

3.2 Definition of Left-Handed Materials

Left-handed materials (LHMs) or negative index materials (NIMs), are materials with simultaneously negative electrical permittivity, ε, and magnetic permeability, μ, and then negative index of refraction, n (Kafesaki, et al., 2007; Veselago, et al., 2006).The negative index of refraction was experimentally verified at low frequencies with LHMs realized from a periodic arrangement of metallic printed lines(or rods) that exhibit a negative permittivity and a periodic array of split-ring resonators (SRRs) that exhibit a negative permeability (Pandey, Kumar, & Thapa). Left-handed materials(LHMs) are defined as artificial effectively homogeneous structures with exotic properties not found in nature (Liu & Zhang, 2011). The condition $p = \lambda_g/4$ refers to as the effective- homogeneity limit or condition, to ensure that refractive phenomena will dominate over scattering/diffraction phenomena when a wave propagates inside the LHM medium.

Where p is the separation between the centers of split ring resonators or between the metallic wires. λ_g is the guided electromagnetic wavelength.

Figure (3.1): First experimental monodimensionally LHM structures consisted of thin continuous wires and SRRs (Pandey, et al.).

3.3 Backward Propagating Waves in LHM

The constitutive parameters of a medium are the electric permittivity ε and magnetic permeability μ, which are related to the index of refraction n by

$$n = \pm\sqrt{|\varepsilon_r||\mu_r|}\,, \qquad 3.1$$

Where ε_r and μ_r are the relative permittivity and permeability related to the free space permittivity and permeability by $\varepsilon_0 = \varepsilon/\varepsilon_r = 8.854 \times 10^{-12}$ C^2/N.m^2 and $\mu_0 = \mu/\mu_r = 4\pi \times 10^{-7}$ Wb/A.m respectively. In equation (3.1) the sign of the square root depends on the signs of ε and μ.

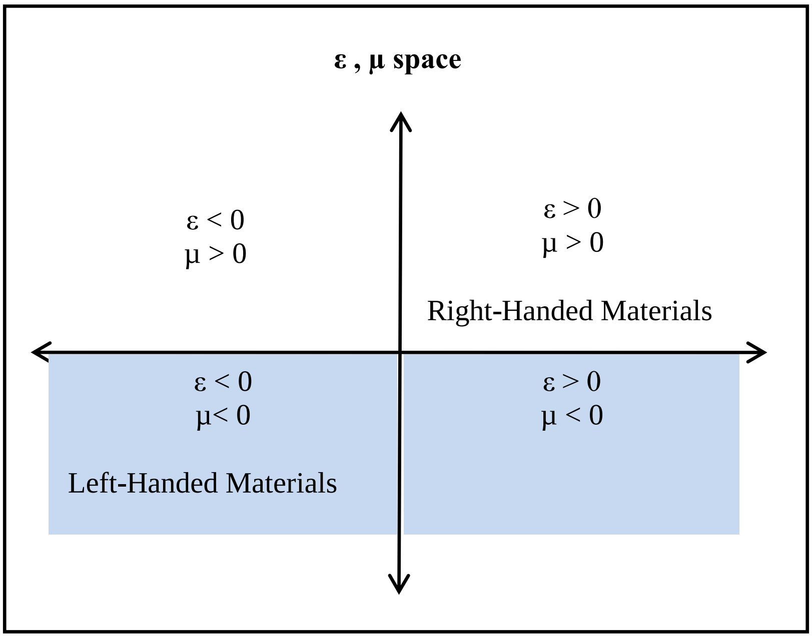

Figure (3.2): Material parameter space can be conveniently visualized on a set of (ε,μ) axes. Materials which possess a positive permeability are represented by points in the upper half plane (Ubeid etal, 2013).

The four possible sign combinations are in the pair(ε and μ) (+,+), (+,-), (-,+) and (-,-) as illustrated the ε and μ diagram of figure 3.2. In the first quadrant (+,+), materials allow forward propagation of waves and are called RHMs. In the second quadrant(+,-), the product μ(ω) ε(ω) is negative, and the refractive index , being the square root of a negative number, leads to a pure imaginary k-value (Ubeid etal, 2013).

An imaginary k implies an evanescent wave, or a wave in which field amplitudes decay exponentially. In the fourth quadrant (-,+) we find a negative product of μ(ω)ε(ω), and k values are pure imaginary as in quadrant (+,-). And, in quadrant (-,-), materials allow backward propagation of waves and are called LHMs. As a consequence of their double negative parameters, they allow backward propagating waves and characterized by negative index of refraction (Smith, Vier et al. 2005; Ubeid et al. 2013).

3.4 Dielectric Properties of LHMs

Assume the motion of a bound electron in the presence of an applied electric field. The equation of motion for an electron of charge –*e* bound by a harmonic oscillatory force and acted on by an applied electric field is

$$m\ddot{x} = eE_0 e^{\,i\omega t} - kx - m\alpha\dot{x}, \qquad 3.2$$

Where k is the force constant (N/m), m =9.11 x 10^{-31} Kg is the mass of electron, e =-1.6 x 10^{-19} C is the charge of electron, and α is a parameter measures the phenomenological damping force. The damping constant α is generally small compared with the resonance or the binding frequency of the electron.

As the electric field varies harmonically in time t with frequency ω as $e^{-i\omega t}$, an electric dipole moment is created as the electric field tries to separate the electron from the positively charged nucleus.

The dipole moment contributed by one electron is (Antipov, Liu et al. 2005):

$$p = -ex = \frac{e^2}{m}(\omega_0^2 - \omega^2 - i\omega\gamma)^{-1}, \qquad 3.3$$

We sum up the individual electric dipole moments to get the net polarization, $P = Nex = \varepsilon_0 \chi E$. Then the dielectric constant is given by:

$$\varepsilon_r(\omega) = \frac{\varepsilon(\omega)}{\varepsilon_0} = 1 + \frac{Ne^2}{\varepsilon_0 m}\sum_j f_j \left(\omega_j^2 - \omega^2 - i\omega\gamma_j\right)^{-1}, \qquad 3.4$$

Where f_j is the number of electrons per molecule with binding(resonance) frequency ω_j and damping constant γ_j.

The electric susceptibility is given by

$$\chi_e = \frac{Ne^2}{\varepsilon_0 m}\sum_j f_j \left(\omega_j^2 - \omega^2 - i\omega\gamma_j\right)^{-1},$$

With suitable quantum-mechanical demonstrations, equation (3.3) represents an accurate description of the atomic contribution to the dielectric constant.

For frequencies far above the highest binding frequency of the electronic contribution the dielectric constant (eq.3.4) takes on the simple form

$$\varepsilon_{r(\omega)} = 1 - \frac{\omega_{pe}^2}{\omega^2}, \qquad 3.5$$

Where ω_{pe} is called the plasma frequency of the medium, which depends only on the total number NZ of electrons per unit volume of a medium.

The thin metallic wires in Left-handed medium have an effective dielectric function given by (Ramakrishna, 2005):

$$\varepsilon_{r(\omega)} = 1 - \frac{\omega_{pe}^2}{\omega^2 - i\omega\alpha}, \qquad 3.6$$

Where the plasma frequency ω_{pe} depends on the geometrical wire array system parameters, namely, the cross-section of the wires and the periodicity of the medium. For mm scale wires the frequency $f_p = \frac{\omega_{pe}}{2\pi}$ falls in the few GHz regime. This permittivity function corresponds to a frequency gap in propagating modes between $\omega = 0$ GHz and $\omega = \omega_{pe}$ the plasma frequency. α is the damping factor due to the metal losses and depends on the medium unit cell size parameters, the conductivity of the metal and the value of the plasma frequency.

The resonant permeability of SRRs is characterized by the generation of resonant loop-like currents, under the influence of an external alternating magnetic field. These loop currents lead to a resonant magnetic dipole moments, and thus to a resonant permeability, has the generic function form (U. C. S. Diego & L. Catherina , 2011) :

$$\mu(\omega) = \mu_0 \left(1 - \frac{F\omega^2}{\omega^2 - \omega_m^2 + i\omega\gamma_m}\right). \qquad 3.7$$

Where $\omega_m = \frac{1}{\sqrt{LC}}$ is the frequency of the magnetic resonance since the loop-current element is a resonant electromagnetic system and very often described as an induction-capacitance (LC) circuit. γ_m is a factor representing the losses. It is worth mentioning that the losses due to LHM contribution affects both the transmitted and reflected powers of any structure containing LHM component.

F is a parameter determines the strength of the magnetic resonance and the width of the negative permeability regime. Hence, it is a geometrical factor which is approximately equal to the volume fraction of the loop-current element within the system unit cell.

3.5 Poynting Vector and Backward Propagation

Helmholtz wave equation yields by combining Maxwell equations and has the form

$$\nabla^2 + \varepsilon\mu\omega^2 \begin{pmatrix} \vec{E} \\ \vec{B} \end{pmatrix} = 0, \qquad 3.8$$

Conventionally, we introduce the electromagnetic wave fields as

$$\vec{\mathrm{E}}(\mathrm{x}, \mathrm{t}) = \vec{\xi} e^{i(k\hat{n}\cdot\vec{x}-\omega t)}, \qquad 3.9$$

$$\vec{B}(x,t) = \vec{\mathfrak{b}}\, e^{i(k\hat{n}\cdot\vec{x}-\omega t)}, \qquad 3.10$$

Where $\vec{\xi}$, $\vec{\mathfrak{b}}, and\ \hat{n}$ divergences are constant vectors. $\hat{n}$ represents the direction of wave propagation such that $\vec{k} = k\hat{n}$.

The divergence Maxwell equations demand that

$$\hat{n} \cdot \overrightarrow{\xi} = 0 \quad and \quad \hat{n} \cdot \vec{\mathfrak{b}} = 0$$

This means that $\vec{E}$ and $\vec{B}$ are both perpendicular to the direction of propagation n. Such a wave is called a transverse electromagnetic wave.

The Poynting vector $\vec{S}$ gives the direction of electromagnetic energy propagation and given as

$$\vec{S} = \vec{E} \times \vec{H}, \qquad 3.11$$

This vector quantity does not depend on ε and μ but only depends on $\vec{\mathrm{E}}$ and $\vec{\mathrm{H}}$.

In fact, the propagation of plane electromagnetic wave through RHMs exhibits parallel pointing and wave vectors. On the other hand, for LHMs, Veselago noticed that the magnetic field, electric field and wave propagation vectors obey a left-handed rule since the pointing and wave vectors are antiparallel vectors.

To explain the reversal of the origin we start with Maxwell equations (Ubeid et al , 2013):

$$\overrightarrow{\nabla} \cdot \vec{D} = 0 \,, \tag{3.12}$$

$$\vec{\nabla} \cdot \vec{B} = 0 \,, \tag{3.13}$$

$$\vec{\nabla} \times \vec{E} = -\frac{\partial \vec{B}}{\partial t} \,, \tag{3.14}$$

$$\vec{\nabla} \times \vec{H} = \frac{\partial \vec{D}}{\partial t} \,. \tag{3.15}$$

Where:

$\vec{E}$: is the electric field intensity (V/m);

$\vec{B}$: is the magnetic induction (Wb/m^2 or T);

$\vec{H}$: is the magnetic field intensity (A/m);

$\vec{D}$: is the electric displacement (C/m^2);

$\vec{J}$: is the electric current density (A/m^2); and

ρ : is the electric charge volume density (C/m^3).

For a uniform, isotropic, linear (ε and μ are independent of E and B, respectively) and dispersive (both ε and μ depend on frequency ω) medium, we have the constitutive relations:

$$B = \mu(\omega) H \qquad and \qquad D = \varepsilon(\omega) E$$

Where ε is the electric permittivity and μ is the magnetic permeability. It should be noted that the detailed properties of a medium's electromagnetic response are contained in ε and μ ,which we refer to as the material parameters.

If we assume solutions with harmonic time dependence $e^{-i\omega t}$, then this allows us to replace Maxwell equations by $-i\omega$ (i.e., $\frac{\partial}{\partial t} \rightarrow -i\omega t$) . After using the constitutive relations in the frequency domain in absence of sources (no charge, no current), the Maxwell equations are:

$$\vec{\nabla} \times \vec{E} = i\omega\mu\vec{H}\,, \qquad 3.16$$

$$\vec{\nabla} \times \vec{H} = -i\omega\mu\vec{E}, \qquad 3.17$$

$$\overrightarrow{\nabla\cdot}\,\vec{D} = 0, \qquad 3.18$$

$$\vec{\nabla} \cdot \vec{B} = 0, \qquad 3.19$$

On the other hand, assuming space dependence of the form $e^{i\vec{k}.r}$ allows us to replace the ∇ operator with $i\vec{k}$. Where $\vec{k}$ is the wave propagation vector. To clarify this, we consider the following:

$$\vec{\nabla}e^{i\vec{k}\cdot r} = \left[\hat{x}\frac{\partial}{\partial x} + \hat{y}\frac{\partial}{\partial y} + \hat{z}\frac{\partial}{\partial z}\right]e^{i\vec{k}\cdot r},$$

$$= \left[\hat{x}\mathrm{i}k_x + \hat{y}\mathrm{i}k_y + \hat{z}\mathrm{i}k_z\right]e^{i\vec{k}\cdot r} = i\vec{k}e^{i\vec{k}\cdot r}.$$

Therefore, Maxwell's curl equations become:

$$\vec{k} \times \vec{E} = \omega\mu\overrightarrow{H}, \qquad 3.20$$

$$\vec{k} \times \vec{H} = -\omega\varepsilon\vec{E}. \qquad 3.21$$

For a plane wave propagation, energy flows in the same direction as the Poynting vector. The Poynting vector forms a right handed system only if the permeability is greater than zero. For negative permeability, the direction of propagation is reversed with respect to the direction of the energy flow. Hence, $\vec{E}, \vec{H}$ and $\vec{K}$ forming a left-handed system. One can stem this from the fact that the curl equation relating $\vec{E}$,$\vec{B}$, and $\vec{K}$ does not change in media where both permeability and permittivity are simultaneously negative.

In a right-handed medium (ε, $\mu > 0$), therefore equations (3.26) and (3.27) build the familiar right-handed triad ($\vec{\mathrm{E}}, \vec{\mathrm{H}}, \vec{\mathrm{K}}$) shown in figure 3.3(a).

In contrast for a left-handed medium ($\varepsilon < 0$, $\mu < 0$), and therefore $\varepsilon = -|\varepsilon|$ and $\mu = -|\mu|$, Maxwell equations take the following form for a plane wave [$\vec{E}$(r), $\vec{H}$(r)]=[$E_0\, e^{-ik\cdot r}, H_0 e^{-ik\cdot r}$]:

$$\vec{\mathrm{k}} \times \vec{E} = -\omega|\mu|\vec{H} \quad and \quad \vec{k} \times \vec{H} = +\omega|\varepsilon|\vec{E}$$

where the harmonic time dependence $e^{-i\omega t}$ is assumed.

Therefore, the triplet($\vec{\mathrm{E}}$, $\vec{\mathrm{H}}$, $\vec{\mathrm{k}}$) builds a left-handed traid, as illustated in figure figure 3.3(b).

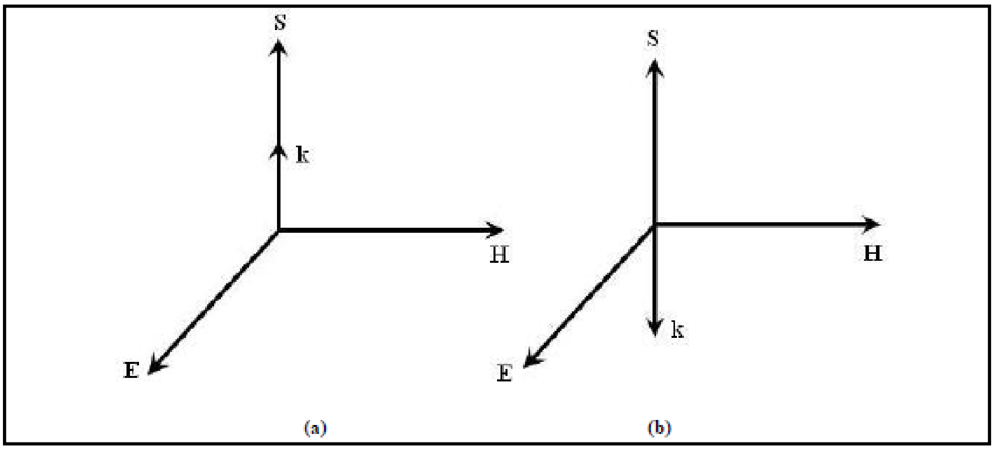

Figure (3.3): Directions of the triads ($\vec{\mathrm{E}}$, $\vec{\mathrm{H}}$, $\vec{\mathrm{k}}$) and ($\vec{\mathrm{E}}$,$\vec{\mathrm{H}}$,$\vec{\mathrm{S}}$) for ; (a) RHM ($\varepsilon,\mu > 0$). (b) LHM ($\varepsilon,\mu < 0$) (Ubeid etal, 2013).

3.6 Phase and Group Velocities in LHMs

In RHMs, the phase velocity is positive since both the wave propagation magnitude k and the frequency ω is greater than zero. The phase velocity is given by (Ubeid et al, 2013):

$$\overrightarrow{V_p} = \frac{\omega}{k}\hat{n} \quad ; \quad \hat{n} = \frac{\vec{n}}{|\vec{n}|} \qquad 3.22$$

Where $\hat{n}$ is the direction of wave propagation.

Now, in LHMs, as a direct consequence of the fact that the Poynting and wave propagation directions are opposite directions, the phase velocity is negative.

The gradient of frequency in the wave propagation space is the group velocity and given by

$$\overrightarrow{V_g} = \overrightarrow{\nabla_k}\,\omega = \frac{\partial\omega}{\partial k_x}\hat{x} + \frac{\partial\omega}{\partial k_y}\hat{y} + \frac{\partial\omega}{\partial k_z}\hat{z} \qquad 3.23$$

In LHMs, the poynting vector associated with the power flowis parallel to the group velocity since it (the Poynting vector) has the same direction of propogation of energy over the time. Hence, the group velocity is always positive in both cases of material handedness.

One can summerize as follows (Ubeid et al, 2013):

$$RHMs: \quad V_p > 0, (k > 0) and\, V_g > 0$$

$$LHMs: \quad V_p < 0, (k < 0) and\, V_g > 0$$

3.7 Negative Sign of the Index of Refraction

In RHM, the wave vector $\vec{k}$ is directed away from the source and toward the source for LHM. Hence, the wave vector k is known to has positive sign in a RHM and negative sign in a LHM.

Suppose that the index of refraction n is complex, and takes the form $n = n_R + \mathrm{i}n_I$. Then, the exponential in the electromagnetic fields written as

$$e^{i\vec{k}_0 n\cdot x - i\omega t} = e^{-\vec{k}_0 n_I \cdot x} e^{i\vec{k}_0 n_R \cdot x - i\omega t} \qquad 3.24$$

The incident electromagnetic wave possesses exponential decay or growth in specific directions. $\vec{k}_0$ represents the wave propagation vector in free space.

The dot product requirement ,$n \cdot n = 1$, results in two parts:

The real part: $n_R^2 - n_I^2 = 1$ and The imaginary part: $n_R \cdot n_I = 0$

The latter shows that n_R and n_I have orthogonal orientations.

For homogeneous (i.e., $n = n_R$) and isotropic medium the wave vector is given by $K = \omega/v = n\omega/c, v$: the phase velocity, $n=\pm\sqrt{\mu_r \varepsilon_r}$, $\mu_r = \mu/\mu_0$ and $\varepsilon_r = \varepsilon/\varepsilon_0$.

In case of left-handedness materials,$\vec{k}$ is negative(i.e., wave and Pointing vectors are anti-parallel). Accordingly, the index of refraction n is negative in a medium with simultaneously negative permeability and permittivity.

3.8 Reversal of Snell's law (Negative Refraction Phenomenon)

Owing to their negative index of refraction, LHMs exhibits a reversed Snell's law when interfaced with RHMs. The statement of the well-known Snell's law (Widom & Drosdoff, 2005) is

$$n_i sin\theta_i = n_r sin\theta_r = n_t sin\theta_t \qquad 3.25$$

Where $n_i = n_r \, and \, \theta_i = \theta_r$.

n_i denotes the medium of wave incidence, the same medium for reflection. n_t denotes the medium where refraction takes place.

θ_i: The angle of incidence,

θ_r: The angle of reflection and

θ_t: The angle of refraction.

Snell's refraction law is modified at the interface between a RHM and a LHM due to the negative sign of the refractive index of the LHM. However, if the two media follow the Left-handedness rule, the mutual cancellation of the two minus signs of the two refractive indices keeps Snell's law invariant. An electromagnetic wave incident upon the interface between two right-handed media experiences conventional positive refraction, characterized by positive angle of refraction, figure 3.4 (a). Whereas, for a wave at the interface between RHM and LHM (different handedness), the refracted wave obeys the reversed Snell law (i.e., $\theta_t < 0$) since it is on the same side of the normal to as the incident wave, figure 3.4 (b) (Ubeid et al, 2013).

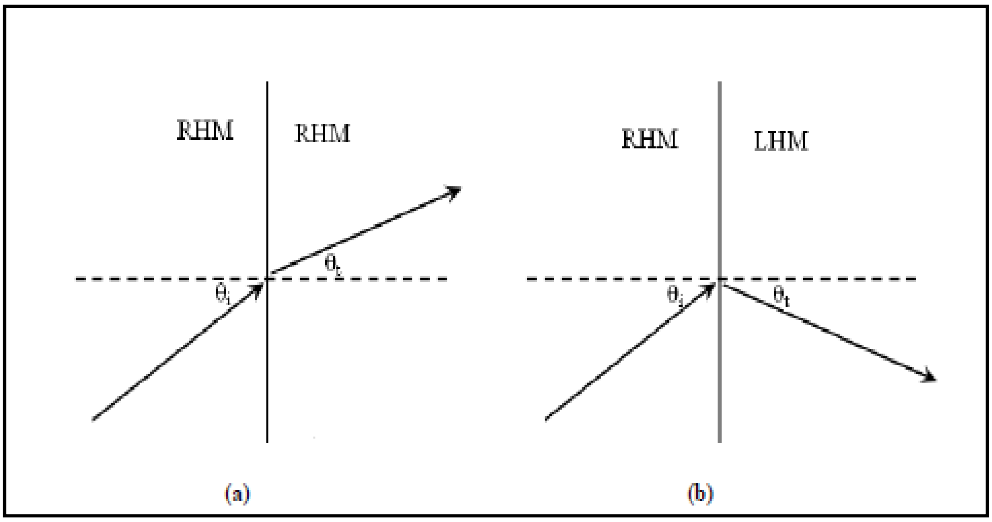

Fig. (3.4): Refraction of an incident electromagnetic wave at the interface between two media. (a) Case of two media of the same handedness (either RHMs or LHMs). (b) Case of two media (one of Right-handedness and the other of Left-handedness) (Ubeid etal, 2013).

.

Chapter 4

Electromagnetic Wave Propagation in DLC-PS-LHM Waveguide Structure

In this chapter, electromagnetic wave propagation through a structure consisting of three layers inserted in vacuum is investigated theoretically and numerically. A transverse electric plane polarized wave plane (TE) incidence on the structure is considered. In section 4.1, the transfer matrix method has been introduced. In this section, Maxwell's equations are used to determine the electric and magnetic fields of the incident waves at each layer of the structure. Also, the boundary conditions are imposed at each interface to obtain a number of equations with unknown parameters. Then, the equations are solved for the unknown parameters to obtain the reflection and the transmission coefficients. These coefficients are used to determine the reflected, transmitted and loss powers of the whole structure. In section 4.2, numerical results on the transmitted, reflected and loss powers of a new structure containing diamond-like carbon, porous silicon and left-handed material (see figure 4.2) as a functions of frequency are presented. In section 4.2.1, the negative refraction of the left-handed materials in the GHz frequency range has been investigated. The effect of the thickness of the left-handed material on the wave propagation of the structure has been viewed in section 4.2.2. In section 4.2.3, the effect of varying the value of the dissipation factor of the left-handed material on wave propagation has been illustrated.

4.1 Theory

In this section, the transfer matrix method is applied in order to derive the characteristic matrix for a structure of three layers. Hence, we have four interfaces. The tangential components of the electric field $\vec{E}$ and magnetic field $\vec{H}$ are continuous across each interface (See figure 4.1).

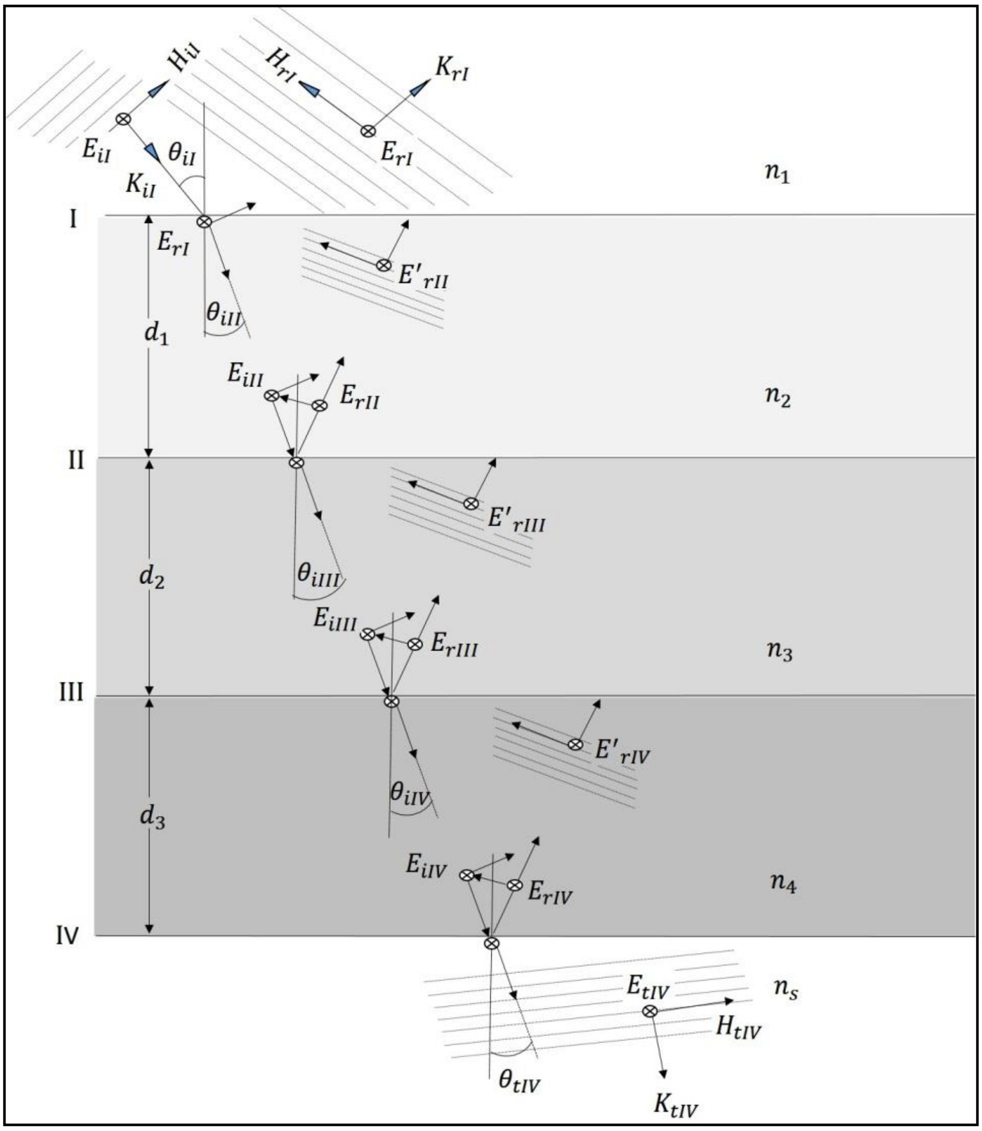

Figure (4.1): TE-Wave propagation through a structure consisting of three slabs inserted in vacuum.

Transfer matrix formulation is given by equations (4.1) through (4.62). Since the studied structure consists of three slabs, it would have four boundaries, namely, I, II, III and IV. Boundary conditions for both the electric and magnetic fields of a transverse electric plane waves incident on the boundaries are introduced as follows:

Boundary I :

$$E_I = E_{iI} + E_{rI} = E_{tI} + E'_{rII}, \qquad 4.1$$

Since the magnetic field

$$\vec{H} = \frac{1}{\mu_r}\sqrt{\frac{\varepsilon_r}{\mu_0}} n\hat{k} \times \vec{E}, \qquad 4.2$$

Where μ_r is the relative magnetic permeability of a material of refractive index given by

$$n = \frac{c}{v} = \sqrt{\frac{\varepsilon\mu}{\mu_0\varepsilon_0}} = \sqrt{\mu_r\varepsilon_r}, \qquad 4.3$$

Then

$$H_I = \frac{1}{\mu_{r1}}\sqrt{\frac{\varepsilon_0}{\mu_0}}(\mathrm{E_{iI}} - \mathrm{E_{rI}})\mathrm{n_1}\cos(\theta_{\mathrm{iI}}) = \frac{1}{\mu_{r2}}\sqrt{\frac{\varepsilon_0}{\mu_0}}(\mathrm{E_{tI}} - \mathrm{E'_{rII}})\mathrm{n_2}\cos(\theta_{\mathrm{iII}}) \qquad 4.4$$

Boundary II :

$$E_{II} = E_{iII} + E_{rII} = E_{tII} + E'_{rIII}, \qquad 4.5$$

$$H_{II} = \frac{1}{\mu_{r2}}\sqrt{\frac{\varepsilon_0}{\mu_0}}\ (E_{iII} - E_{rII})n_2 Cos(\theta_{iII})$$

$$= \frac{1}{\mu_{r3}}\sqrt{\frac{\varepsilon_0}{\mu_0}}\ \left(E_{tII} - E'_{rIII}\right)n_3 Cos(\theta_{iIII}). \qquad 4.6$$

Boundary III :

$$E_{III} = E_{iIII} + E_{rIII} = E_{tIII} + E'_{rIV}\ , \qquad 4.7$$

$$H_{III} = \frac{1}{\mu_{r3}}\sqrt{\frac{\varepsilon_0}{\mu_0}}\ (E_{iIII} - E_{rIII})n_3 Cos(\theta_{iIII})$$

$$= \frac{1}{\mu_{r4}}\sqrt{\frac{\varepsilon_0}{\mu_0}}\ \left(E_{tIII} - E'_{rIV}\right)n_4 Cos(\theta_{iIV}). \qquad 4.8$$

Boundary IV:

$$E_{IV} = E_{iIV} + E_{rIV} = E_{tIV}, \qquad 4.9$$

$$H_{IV} = \frac{1}{\mu_{r4}}\sqrt{\frac{\varepsilon_0}{\mu_0}}(E_{iIV} - E_{rIV})n_4 Cos(\theta_{iIV}) = \frac{1}{\mu_{r5}}\sqrt{\frac{\varepsilon_0}{\mu_0}}E_{tIV}n_5 Cos(\theta_{tIV}), \qquad 4.10$$

Now consider

$$\left(n_2 d_1 Cos(\theta_{iII})\right) = h_1, \qquad 4.11$$

Therefore

$$E_{iII} = E_{tI}e^{ik_0h_1}, \qquad 4.12$$

and

$$E_{rII} = E'_{rII}e^{-ik_0h_1}, \qquad 4.13$$

The boundary conditions at boundary II are

$$E_{II} = E_{tI}e^{ik_0h_1} + E'_{rII}e^{-ik_0h_1}, \qquad 4.14$$

and

$$H_{II} = \frac{1}{\mu_{r2}}\sqrt{\frac{\varepsilon_0}{\mu_0}}\left(E_{tI}e^{ik_0h_1} - E'_{rII}e^{-ik_0h_1}\right)n_2 Cos(\theta_{iII}), \qquad 4.15$$

Solving for E_{t1} by adding 4.14 and 4.15 yields

$$E_{\mathrm{t1}} = \frac{1}{2}(E_{II} + \frac{H_{II}}{\gamma_1})\mathrm{e}^{-\mathrm{i}\,k_0 h_1}, \qquad 4.16$$

Solving for E'_{rII} by subtracting 4.14 and 4.15 yields

$$E'_{rII} = \frac{1}{2}(E_{II} - \frac{H_{II}}{\gamma_2})\mathrm{e}^{+\mathrm{i}\,k_0 h_1}, \qquad 4.17$$

Substituting from 4.16 and 4.17 back into 4.1 for boundary I yields

$$E_I = \frac{1}{2}(E_{II} + \frac{H_{II}}{\gamma_2})\mathrm{e}^{-\mathrm{i}k_0 h_1} + \frac{1}{2}(E_{II} - \frac{H_{II}}{\gamma_2})\mathrm{e}^{+\mathrm{i}\,k_0 h_1}, \qquad 4.18$$

or

$$E_I = E_{II}\cos k_0 h_1 - i\frac{H_{II}}{\gamma_2}\sin k_0 h_1, \qquad 4.19$$

Substituting from 4.16 and 4.17 back into 4.4 for boundary I yields

$$H_I = \left(\frac{1}{2}(E_{II} + \frac{H_2}{\gamma_2})\mathrm{e}^{-\mathrm{i}\,k_0 h_1} - \frac{1}{2}(E_{II} - \frac{H_{II}}{\gamma_2})\mathrm{e}^{+\mathrm{i}\,k_0 h_1}\right)\gamma_1, \qquad 4.20$$

or

$$H_1 = -i\,E_{II}\gamma_2 \sin k_0 h_1 + H_{II}\cos k_0 h_1, \qquad 4.21$$

where

$$\gamma_2 = \frac{1}{\mu_{r2}}\sqrt{\frac{\varepsilon_0}{\mu_0}}n_2 Cos(\theta_{iII}), \qquad 4.22$$

In matrix notation, equations 4.19 and 4.21 can be represented as

$$\begin{pmatrix} E_I \\ H_I \end{pmatrix} = \begin{pmatrix} Cos(k_0 h_1) & -iSin(k_0 h_1)/\gamma_2 \\ -\gamma_2 iSin(k_0 h_1) & Cos(k_0 h_1) \end{pmatrix} \cdot \begin{pmatrix} E_{II} \\ H_{II} \end{pmatrix}, \qquad 4.23$$

or

$$\begin{pmatrix} E_I \\ H_I \end{pmatrix} = M_I \cdot \begin{pmatrix} E_{II} \\ H_{II} \end{pmatrix}, \qquad 4.24$$

where M_I is the characteristic matrix which relates the field at two adjacent boundaries.

Likewise, consider

$$n_3 d_2 Cos(\theta_{iIII}) = h_2, \qquad 4.25$$

Therefore

$$E_{iIII} = E_{tII} e^{ik_0 h_2}, \qquad 4.26$$

and

$$E_{rIII} = E'_{rIII} e^{-ik_0 h_2}, \qquad 4.27$$

The boundary conditions at boundary III can be written as

$$E_{III} = E_{tII} e^{ik_0 h_2} + E'_{rIII} e^{-ik_0 h_2}, \qquad 4.28$$

$$H_{III} = \frac{1}{\mu_{r3}} \sqrt{\frac{\varepsilon_0}{\mu_0}} \left(E_{tII} e^{ik_0 h_2} - E'_{rIII} e^{-ik_0 h_2} \right) n_3 Cos(\theta_{iIII}), \qquad 4.29$$

Solving the last two equations for E_{tII} and E'_{rIII} and substituting into Equations 4.5 and 4.6 for boundary II yields

$$E_{II} = E_{III} Cos(k_0 h_2) - \frac{H_{III}(iSin(k_0 h_2))}{\gamma_3}, \qquad 4.30$$

and

$$H_{II} = -E_{III} \gamma_3 i\, Sin(K_0 h_2) + H_{III} Cos(k_0 h_2), \qquad 4.31$$

where

$$\gamma_3 = \frac{1}{\mu_{r3}}\sqrt{\frac{\varepsilon_0}{\mu_0}}n_3 Cos(\theta_{iIII}), \qquad 4.32$$

In matrix representation, we have

$$\begin{pmatrix} E_{II} \\ H_{II} \end{pmatrix} = \begin{pmatrix} Cos(k_0 h_2) & -iSin(k_0 h_2)/\gamma_3 \\ -\gamma_3 iSin(k_0 h_2) & Cos(k_0 h_2) \end{pmatrix}, \qquad 4.33$$

or

$$\begin{pmatrix} E_{II} \\ H_{II} \end{pmatrix} = M_{II} \cdot \begin{pmatrix} E_{III} \\ H_{III} \end{pmatrix}, \qquad 4.34$$

where M_{II} is the characteristic matrix which relates the field at the boundaries II and III.

For boundary III consider

$$n_4 d_3 Cos(\theta_{iIV}) = h_3, \qquad 4.35$$

Therefore

$$E_{iIV} = E_{tIII} e^{ik_0 h_3}, \qquad 4.36$$

and

$$E_{rIV} = E'_{rIV} e^{-ik_0 h_3}. \qquad 4.37$$

The boundary conditions at boundary IV are

$$E_{IV} = E_{tIII} e^{ik_0 h_3} + E'_{rIV} e^{-ik_0 h_3}, \qquad 4.38$$

$$H_{IV} = \frac{1}{\mu_{r4}}\sqrt{\frac{\varepsilon_0}{\mu_0}}\left(E_{tIII} e^{ik_0 h_3} - E'_{rIV} e^{-ik_0 h_3}\right) n_4 Cos(\theta_{iIV}), \qquad 4.39$$

Solving the last two equations for E_{tIII} and E'_{rIV} and substituting into Equations 4.7 and 4.8 for boundary III yields

$$E_{III} = E_{IV} Cos(k_0 h_3) - \frac{H_{IV} i Sin(k_0 h_3)}{\gamma_4}, \tag{4.40}$$

and

$$H_{III} = -E_{IV} \gamma_4 i\ Sin(K_0 h_3) + H_{IV} Cos(k_0 h_3), \tag{4.41}$$

where

$$\gamma_3 = \frac{1}{\mu_{r4}} \sqrt{\frac{\varepsilon_0}{\mu_0}} n_4 Cos(\theta_{iIV}), \tag{4.42}$$

In matrix notation,

$$\begin{pmatrix} E_{III} \\ H_{III} \end{pmatrix} = \begin{pmatrix} Cos(k_0 h_3) & -iSin(k_0 h_3)/\gamma_4 \\ -\gamma_4 i Sin(k_0 h_3) & Cos(k_0 h_3) \end{pmatrix} \cdot \begin{pmatrix} E_{IV} \\ H_{IV} \end{pmatrix}, \tag{4.43}$$

or

$$\begin{pmatrix} E_{III} \\ H_{III} \end{pmatrix} = M_{III} . \begin{pmatrix} E_{IV} \\ H_{IV} \end{pmatrix}, \tag{4.44}$$

where M_{III} is the characteristic matrix relates the field at the boundaries III and IV .

For three overlaying slabs situated in vacuum we write

$$\begin{pmatrix} E_I \\ H_I \end{pmatrix} = M_I M_{II} M_{III} \begin{pmatrix} E_{IV} \\ H_{IV} \end{pmatrix}, \tag{4.45}$$

or

$$\begin{pmatrix} E_I \\ H_I \end{pmatrix} = M \begin{pmatrix} E_{IV} \\ H_{IV} \end{pmatrix}, \tag{4.46}$$

where $M = M_I M_{II} M_{III}$. M is the characteristic matrix that relates the fields at the boundaries I and IV.

Combining equations 4.1,4.4,4.5,4.6,4.7, 4.8, 4.9, 4.10 and 4.46 yields

$$\begin{pmatrix} E_{iI} + E_{rI} \\ (E_{il} - E_{rI})\gamma_1 \end{pmatrix} = \begin{pmatrix} m_{11} & m_{12} \\ m_{21} & m_{22} \end{pmatrix} . \begin{pmatrix} E_{tIV} \\ E_{tIV}\gamma_5 \end{pmatrix}, \qquad 4.47$$

Such that

$$M = \begin{pmatrix} m_{11} & m_{12} \\ m_{21} & m_{22} \end{pmatrix}, \qquad 4.48$$

or

$$E_{iI} + E_{rI} = m_{11}E_{tIV} + m_{12}E_{tIV}\gamma_5 \ , \qquad 4.49$$

and

$$(E_{iI} - E_{rI})\gamma_1 = m_{21}E_{tIV} + m_{22}E_{tIV}\gamma_5 \ , \qquad 4.50$$

where

$$\gamma_1 = \frac{1}{\mu_{r1}} \sqrt{\frac{\varepsilon_0}{\mu_0}} n_1 Cos(\theta_{iI}), \qquad 4.51$$

and

$$\gamma_5 = \frac{1}{\mu_{r5}} \sqrt{\frac{\varepsilon_0}{\mu_0}} n_5 Cos(\theta_{IV}). \qquad 4.52$$

Let

$$r = \frac{E_{rI}}{E_{iI}}, \qquad 4.53$$

and

$$t = \frac{E_{tIV}}{E_{iI}}, \tag{4.54}$$

Then

$$1 + r = m_{11}t + m_{12}\gamma_5 t, \tag{4.55}$$

and

$$(1 - r)\gamma_1 = m_{21}t + m_{22}\gamma_5 t, \tag{4.56}$$

Solving equations 4.55 and 4.56 for r and t yields

$$r = -1 - \frac{2\gamma_1(-m_{11} - m_{12}\gamma_5)}{m_{21} + m_{11}\gamma_1 + m_{22}\gamma_5 + m_{12}\gamma_1\gamma_5}, \tag{4.57}$$

and

$$t = \frac{2\gamma_1}{m_{21} + m_{11}\gamma_1 + m_{22}\gamma_5 + m_{12}\gamma_0\gamma_5}, \tag{4.58}$$

For an electromagnetic waves incident on a structure, we only need to compute the characteristic matrix *M* and substitute the matrix elements into equations 4.57 and 4.58.

The transmitted, reflected and loss power are respectively given by

$$T = \frac{k_{5z}\mu_1}{k_{1z}\mu_5}|t|^2, \tag{4.59}$$

$$R = |r|^2, \tag{4.60}$$

and

$$P_{loss} = 1 - (T + R). \tag{4.61}$$

The statement of the conservation law of energy implies that

$$T + R + P_{loss} = 1. \tag{4.62}$$

Where P_{loss} is the loss power of the whole structure. In eqn.4.59, k_{1z} and k_{5z} stands for the z-components of the wave vector $\vec{k}$ for the first and the fifth (last) media, respectively.

4.2 Numerical Results

In this section the transmitted, reflected and loss powers of a multi-structure are calculated numerically as a function of frequency under the variation of the values of the thickness of slabs, angle of incidence and loss factor. The considered multistructure consists of DLC, PS and LHM, respectively, see figure 4.2.

For the LHM in region 4, the relative permittivity ε_r and the relative permeability μ_r are given by the dispersion relations (Park, Lee, Fu, & Zhang, 2005; C. Yan, Wang, & Cui, 2010):

$$\varepsilon_r(\omega) = 1 - \frac{F_e \omega_{ep}^2}{\omega^2 - \omega_{eo}^2 - i\omega\gamma_e}, \qquad 4.63$$

$$\mu_r(\omega) = \left(1 - \frac{F_m \omega_{mp}^2}{\omega^2 - \omega_{mo}^2 + i\omega\gamma_m}\right), \qquad 4.64$$

where ω_{ep} and ω_{mp} are the electric and magnetic plasma frequencies, ω_{eo} and ω_{mo} are the electric and magnetic resonant frequencies. F_e and F_m are the scaling filling parameters. γ_e and γ_m are the electric and magnetic dissipation factors.

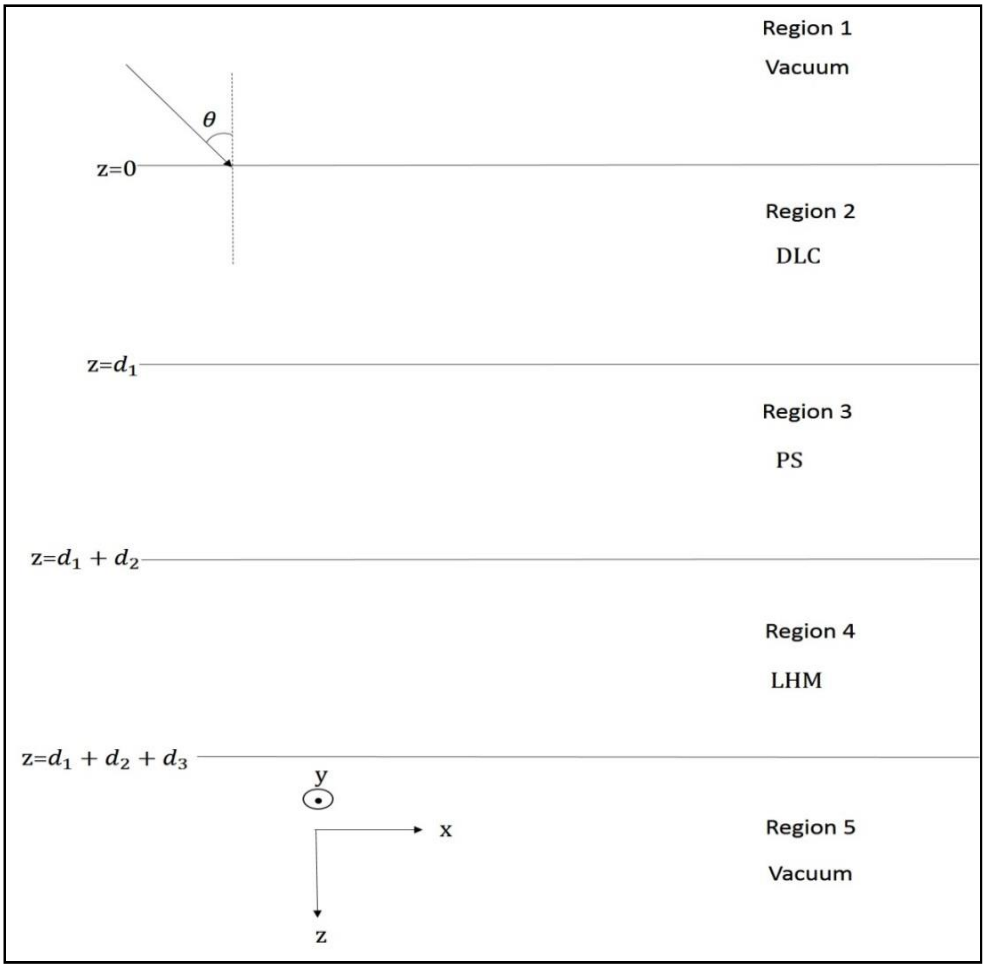

Figure (4.2): Oblique incidence of electromagnetic wave on DLC,PS and LHM structure embedded in vacuum.

In our study, we apply the transfer matrix approach to calculate the transmitted, reflected and loss powers of the new structure. In particular, we aim to examine the effect of adding DLC/PS double layer to a LHM slab. In calculations we have used the parameters for the LHM slab as in (Shabat, Ubeid, & Sid-Ahmed, 2014): ω_{mp}= 2π 10.95 GHz, ω_{mo}= 2π 10.1 GHz, F_m= 0.26, ω_{ep}= 2π 13.3 GHz, ω_{eo}= 2π 10.3 GHz, F_e= .37. For simplicity, the electric and magnetic dissipation factors are selected to be equal to each other ($\gamma_e = \gamma_m = \gamma$) and two cases of the LHM are studied, loss-less case (γ = 0 GHz) and loss case ($\gamma \neq 0$ GHz) .As for the DLC and PS, we based on Ref. (Aroutiounian, Martirosyan, & Soukiassian, 2004) for the selection of the refractive index and thickness values.

4.2.1. Negative Refraction of LHMs

According to equations (4.63) and (4.64), Figure 4.4 shows simultaneously negative permittivity and permeability, and then the refractive index is negative real of the LHM in the frequency range (10.3 GHz – 11.5 GHz). At 10.1 and 10.2GHz frequencies the permeability is positive and the permittivity is negative, and then the refractive index is imaginary which results in zero transmission at these frequencies. The other remaining frequencies perform a transmission through the left handed slab (see figure4.3) since they have simultaneously positive permittivity and permeability, and then the refractive index is real of the LHM.

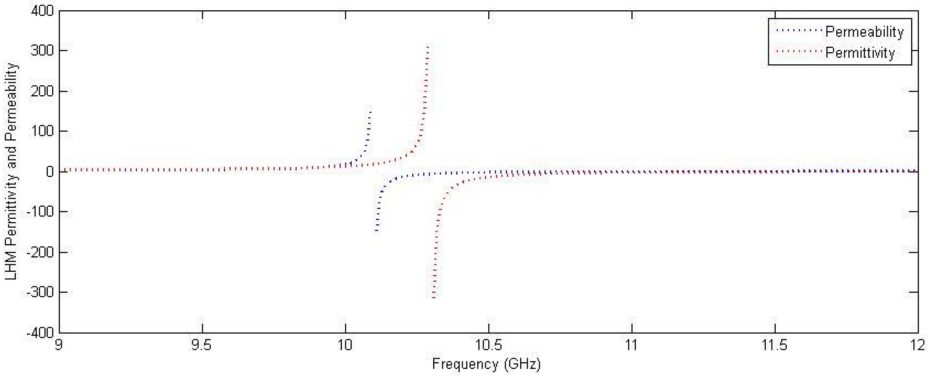

Figure (4.3): Calculated LHM permittivity and permeability versus frequency (9 GHz -12 GHz).

In figure 4.4, the transmitted and reflected powers are plotted as a function of frequency for normal incidence (i.e., $\theta = 0^\circ$) for three types of layered structure as assigned in the figure. The frequency changes between 10.3 GHz and 11.5 GHz since both the permittivity and permeability of the LHM have simultaneously negative values in this range. The loss-less case is considered. The parameters used are the following: ($d_{DLC} = d_{PS}$ = 10 mm, n_{DLC} =1.6 , n_{PS}= 2.9 , γ = 0.0 GHz and θ =0°) where the symbols d and n stand for the thickness and the refractive index of slab, respectively. The subscripts denote the medium.

A sinusoidal behavior of the reflected power versus frequency for is shown in figure 4.4. As evident in the figure, the effect of laying the DLC/PS double layer with mm scale thickness over a LHM slab (red plot) is portrayed as a shift of the green plot (LHM) to the left. This shift is accompanied by broadening in peaks along the frequency range (10.32-11.2 GHz). In the figure, for the frequency range (10.3-10.4 GHz), the bold red color is actually due to the occurrence of multiple resonances.

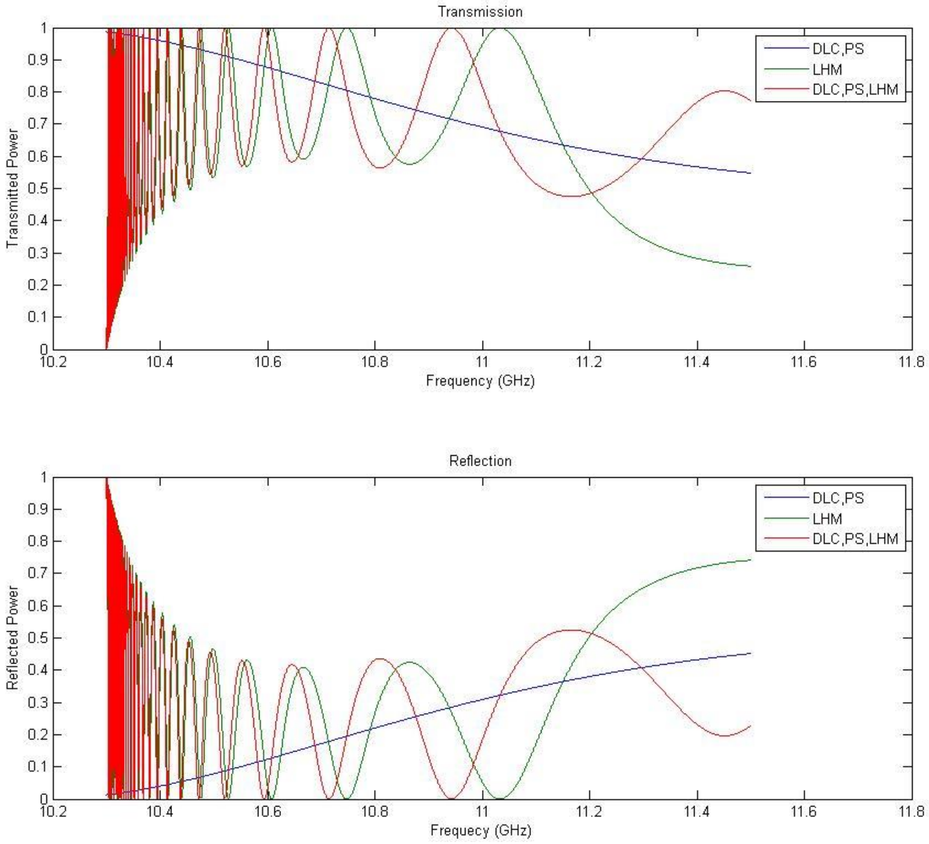

Figur (4.4): Transmitted, reflected powers and their total sum against frequency (10.3 - 11.5 GHz) for $\theta = 0^{\circ}$. ($d_{\mathrm{DLC}} = d_{\mathrm{PS}} = d_{\mathrm{LHM}}$ =10 mm, n_{DLC} =1.6, n_{PS}=2.9, $\gamma = 0.0$ GHz).

Figure 4.5 illustrates the transmitted and reflected powers versus frequency in the loss-less case for both angles ($\theta = 0^\circ$ and $\theta = 30^\circ$).The value of the thickness of each of DLC, PS and LHM slabs is the same and selected to be 13.64 mm. The refractive index of the DLC slab is selected to be 2.7 and that of PS to be 1.25. A conspicuous feature is that we have a resonance peak at 11.38 GHz for 30°angle of incidence while it disappears for normal incidence. The transmitted power against frequency performs a sinusoidal behavior that becomes squeezed as we move to the left accompanied by a gradual increase in the height of power peaks. Also, there are many oscillations within the narrow range of frequency (10.4 - 10.6 GHz).

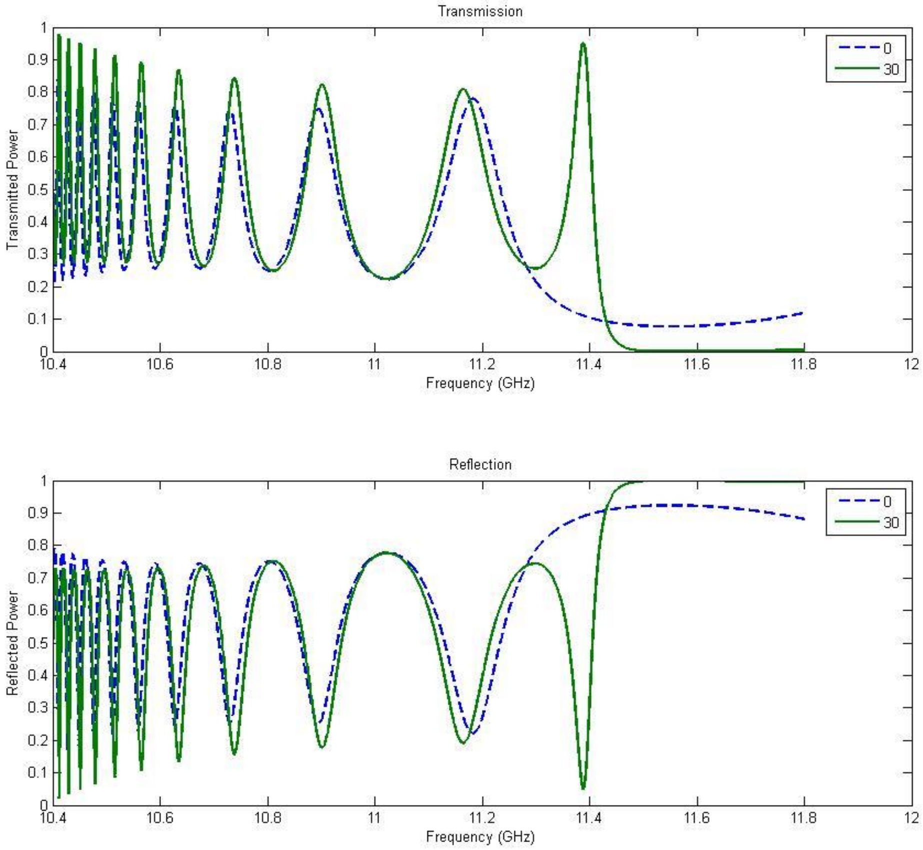

Figure (4.5): Transmitted and reflected powers against frequency (10.3 –10.32 GHz) for different angles of incidence ($\theta = 0^\circ$and $\theta = 30^\circ$). ($d_{\mathrm{DLC}} = d_{\mathrm{PS}} = d_{\mathrm{LHM}}$ =13.64 mm, n_{DLC} =2.7, n_{PS}=1.25, $\gamma = 0.0$ GHz).

In figure 4.6, the transmitted and reflected powers are plotted versus the frequency for two distinct cases of structure, each of them is assigned by certain plot coloring (green / blue) as shown in the figure. It is clear that the left-handed material as a single layer exhibits a better sinusoidal transmission than the tri-layered structure at most of frequencies. However, they match in the frequency range (11.5 - 11.8 GHz) and produce a null transmission.

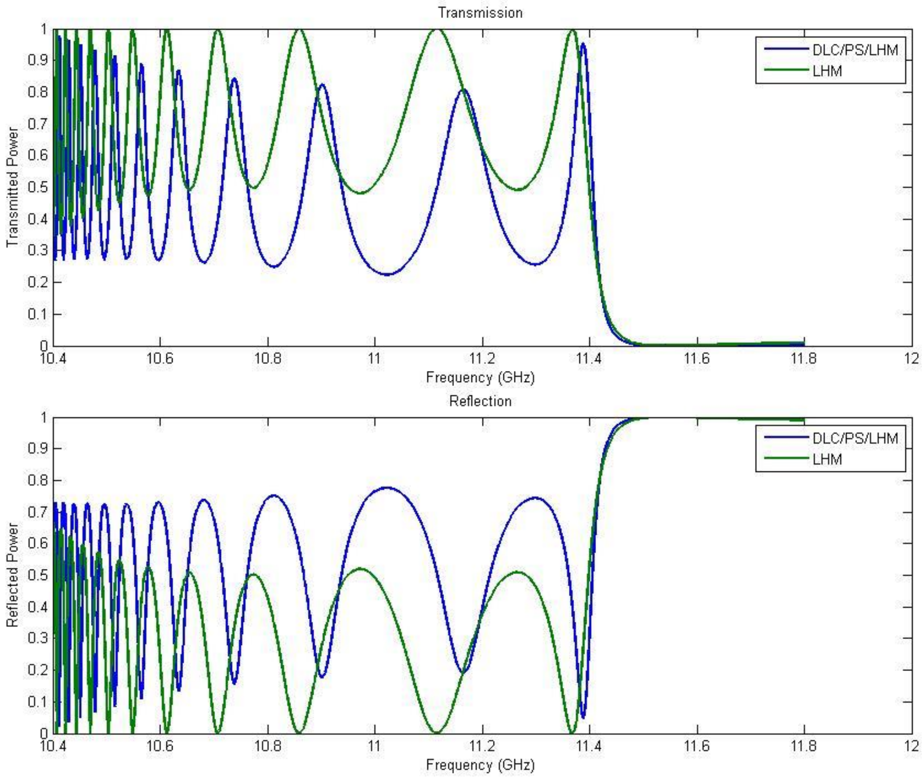

Figure (4.6): Transmitted &reflected powers against frequency (10.4- 11.8 GHz) for angle of incidence (θ = 30˚) for different structures (DLC/PS/LHM) tri-layer and LHM single layer). The data used are:($d_{\mathrm{DLC}} = d_{\mathrm{PS}} = d_{\mathrm{LHM}}$ =13.64 mm, n_{DLC} =2.7, n_{PS}=1.25, γ = 0.0 GHz).

In Figure 4.7, the reflected and transmitted powers versus frequency for the loss-less case are plotted for the following angles (θ = 0˚, θ = 30˚ and θ = 60˚). The thickness of each of the DLC, PS and LHM slabs is selected to be equal 6.82 mm. By comparison with figure 4.5, for both the normal and the oblique incidence, we can observe the effects of lowering the thicknesses of the slabs and increasing the refractive index of PS (to be 3) in minimizing the number of oscillations and broadening the transmission peaks.

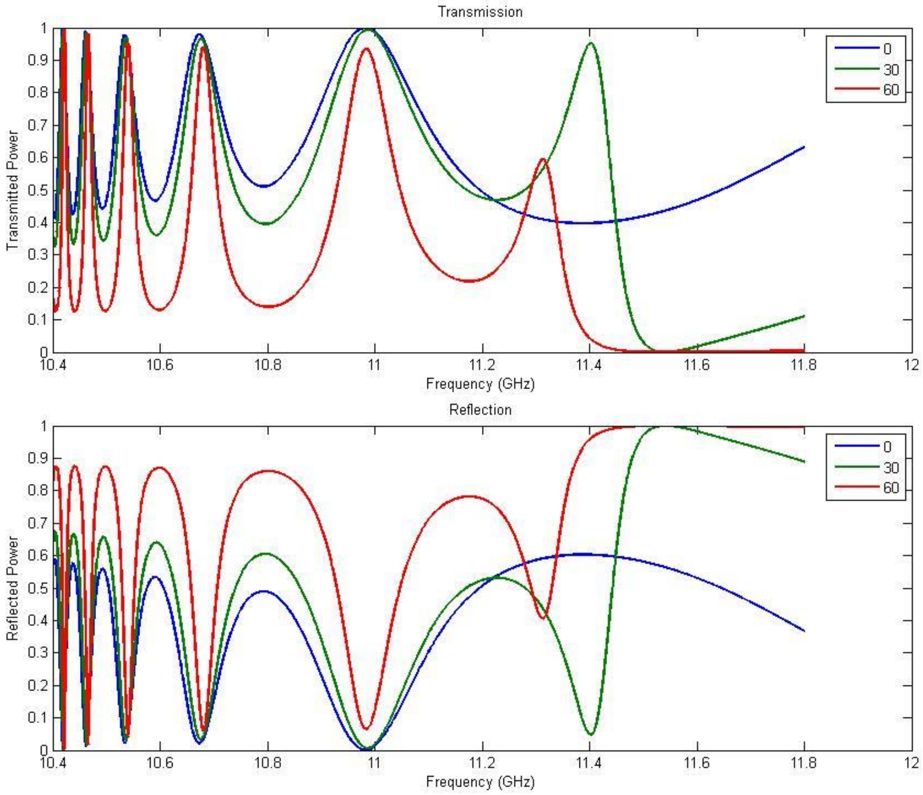

Figure (4.7): Transmitted and reflected powers against frequency (10.4- 11.8 GHz) for different angles of incidence (θ = 0˚, θ = 30˚, θ = 60˚). ($d_{\mathrm{DLC}} = d_{\mathrm{PS}} = d_{\mathrm{LHM}}$ =6.82 mm, n_{DLC} =2.7, n_{PS} =3, γ = 0.0 GHz).

In figure 4.8, the transmitted, reflected and loss powers are plotted against frequency for two distinct case of structure. For the transmitted power, at 10.5 GHz the red and blue starts deviating from each other and meets at certain frequencies. At very low frequency the red and blue plots have same transmitted power while at higher frequency the blue mostly exhibits higher transmitted power than the red. A maximum transmitted power (0.9) is seen for the blue at 11.3 GHz. For the sinusoidal behavior of reflected power, from frequency 10.4 GHz upto 11 GHz the red has lower reflected power than the blue for most frequencies while from the frequency 11 GHz upto 11.8 GHz red has higher reflected power than the blue. However, at certain frequencies, both red and blue match. For the loss power, both plots slightly deviate from each other and they are decreasing sinusoidally with the increase of frequency. For both plots, the loss power is considerable and seems to be extremely high in the range from 10.4 GHz up to 10.6 GHz.

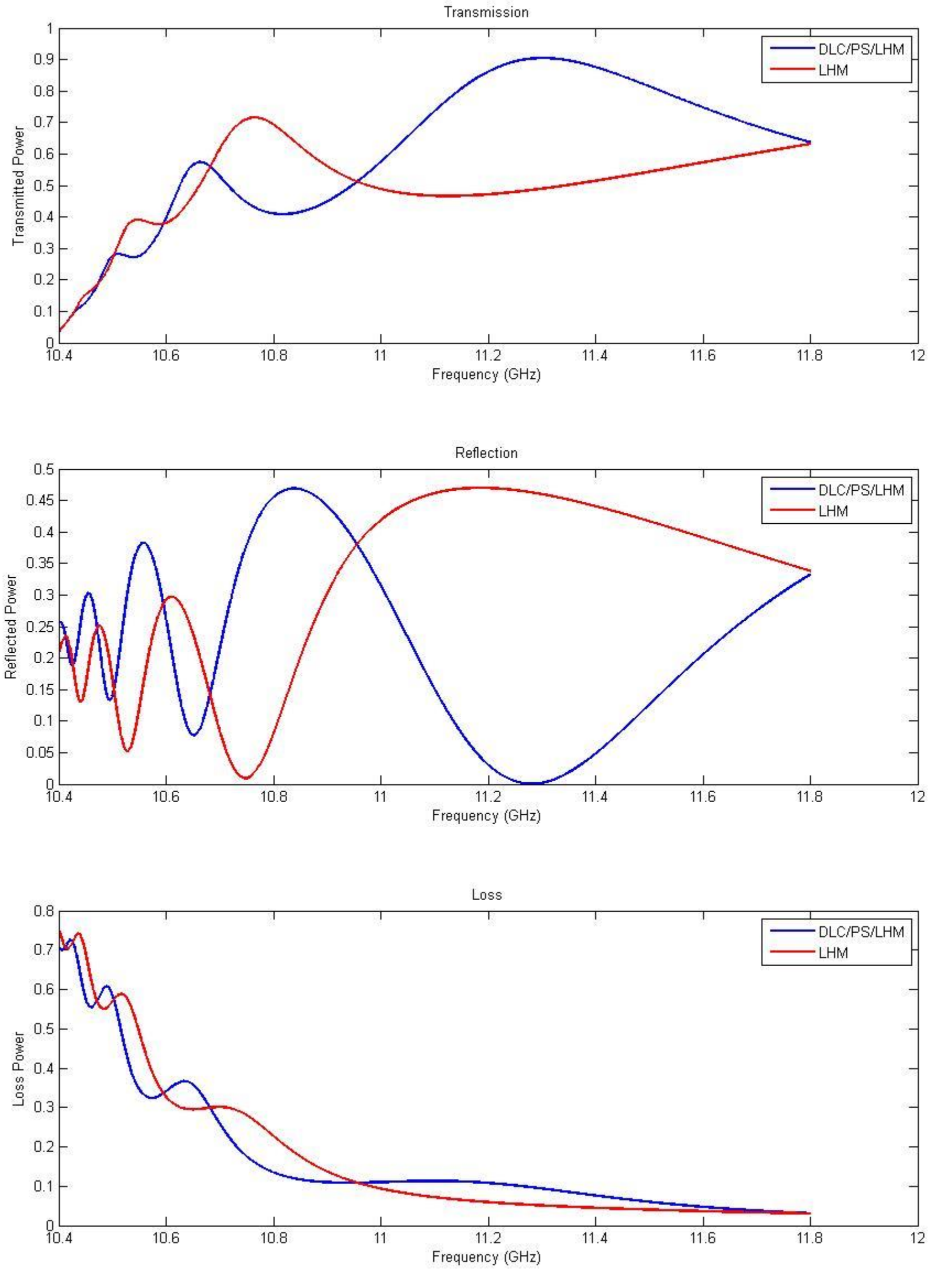

Figure (4.8): Transmitted, reflected and loss powers as a function of frequency (10.4-11.8 GHz) for various angles of incidence ($\theta=0^{\circ}$) for different structures (DLC/PS/LHM) tri-layer and LHM single layer). (d_{DLC} = d_{PS} =1 mm, d_{LHM} =5 mm, n_{DLC} =1.6, n_{PS} =2.9, γ =0.2 GHz).

In figure 4.9, each of the transmitted, reflected and loss powers seemingly behave in a similar oscillatory manner versus the frequency. Despite they deviate from each other along the frequency axis, the two plots do overlap at certain frequencies. Also, a maximum of transmitted power (0.7) is attained near the 11.2 GHz.

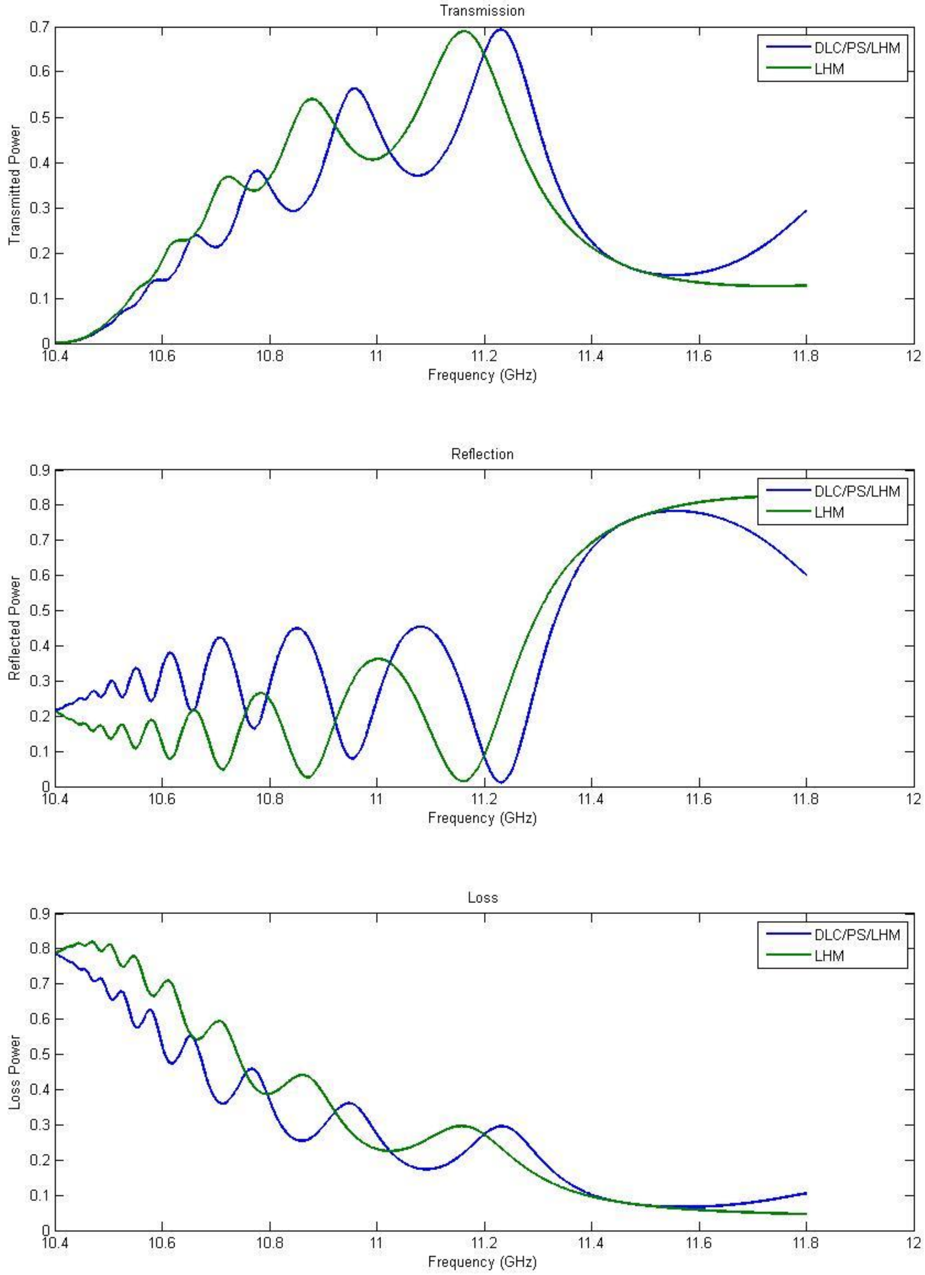

Figure (4.9): Transmitted, reflected and powers against frequency (10.4- 11.8 GHz) for normal incidence ($\theta = 0^\circ$) for different structures ((DLC/PS/LHM) tri-layer and LHM single layer). The data used are :($d_{\mathrm{DLC}} = d_{\mathrm{PS}} = d_{\mathrm{LHM}}$ =13.64 mm, n_{DLC} =2.7, n_{PS} =3, γ = 0.2 GHz).

4.2.2 Effect of the thickness of LHM slab on transmitted, reflected and loss powers of a structure consisting of DLC, PS and LHM

Figure 4.10 confirms the variation of the transmitted, reflected and loss powers with the thickness of the LHM slab in the DLC/PS/LHM structure for the normal incidence case. The loss case (γ =0.2 GHz) is considered. The LHM slab thickness takes the following values: 0 mm,20 mm, 40 mm, 60 mm and 100 mm. The frequency changes between 10.4 GHz and 11.8 GHz. In fact, it is worth mentioning that the oscillatory behaviors of the powers are only attributed to the contribution of the LHM since the thicknesses of the DLC and PS layers are not comparable to the incoming wavelengths.

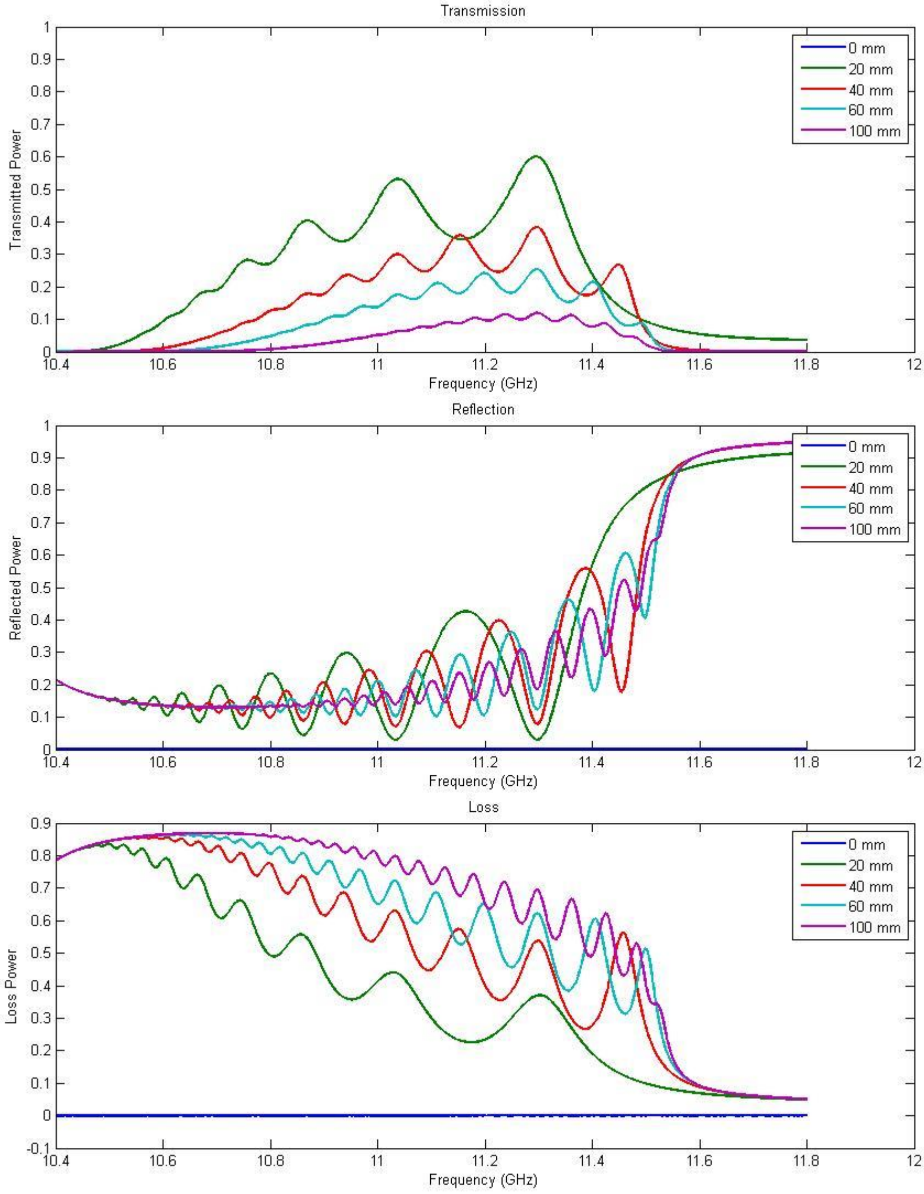

Figure (4.10): Transmitted, reflectted and loss power as a function of frequency (10.4-11.8GHz) for various thicknesses of LHM slab: (d_{LHM}= 0/20/40/60/100 mm). (d_{DLC} = 85 nm, d_{PS} =30 nm, n_{DLC} =1.6 n_{PS} =2.9, γ = 0.2 GHz).

Figure 4.11 presents the transmitted, reflected and loss power versus frequency (9-12 GHz) for 30˚ angle of incidence for two cases of similar thickness slabs. One case for d_{DLC}= d_{PS}= d_{LHM}= 6.82 mm and the other for d_{DLC}= d_{PS}= d_{LHM}= 13.64 mm. The refractive index is 1.6 for the DLC and 2.8 for the PS. The loss case is considered (γ

= 0.1 GHz). As evident in the figure, for 6.82 mm, the transmitted power is higher and the loss power is lower than those for the 13.64 mm case at most frequencies. However, the loss curves do not significantly differ from one another and they present high losses around 10.5 GHz.

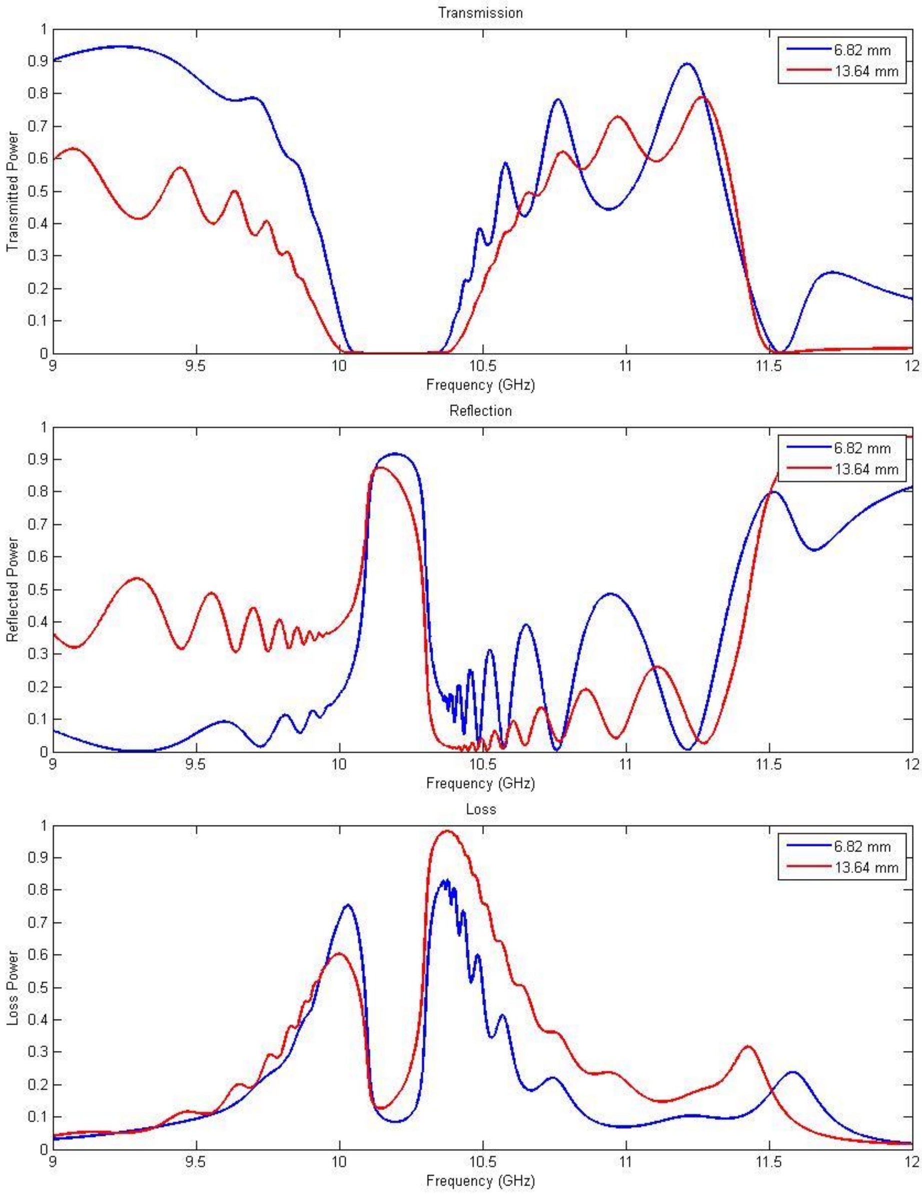

Figure (4.11): Transmitted, reflected and loss Power against frequency (9-12 GHz) for two different values of equal thicknesses of DLC, PS and LHM slabs(d =6.82mm, d =13.64 mm). (n_{DLC} =1.6, n_{PS} =2.8, $\theta = 30^{\circ}$, γ = 0.2 GHz).

4.2.3 Effect of dissipation factor on the transmission of structure consisting of DLC, PS and LHM

Figure 4.12 verifies the effect of the losses due to the LHM slab on the transmitted, reflected and loss powers of the whole structure at the angle of incidence (θ = 45˚). Again, the electric and magnetic dissipation factors are chosen to be the same. The dissipation factor takes the values 0, 0.1 and 0.2 GHz respectively. The thickness of the DLC slab is 85 nm and that of PS is 30 nm. The LHM slab 30 mm thick. The refractive index of the DLC slab is selected to be 1.6 and that of PS is 2.8. As confirmed from the figure, for γ=0.0 GHz , the loss power is null. It is also evident that when the value of loss factor increases, the loss power increases. On the other hand, it is noticed that both the transmitted and the reflected powers decrease as the loss increases. However, for certain vicinities of frequency, the plots are indistinguishable. For the lossless case, for frequency (10.3-10.5 GHz), there is enormous number of resonant peak that vanish for the loss case. Figure 4.13 portrays the effect of losses for the case of similar thicknesses of slabs: $d_{DLC} = d_{PS} = d_{LHM} = 6.82$ mm.

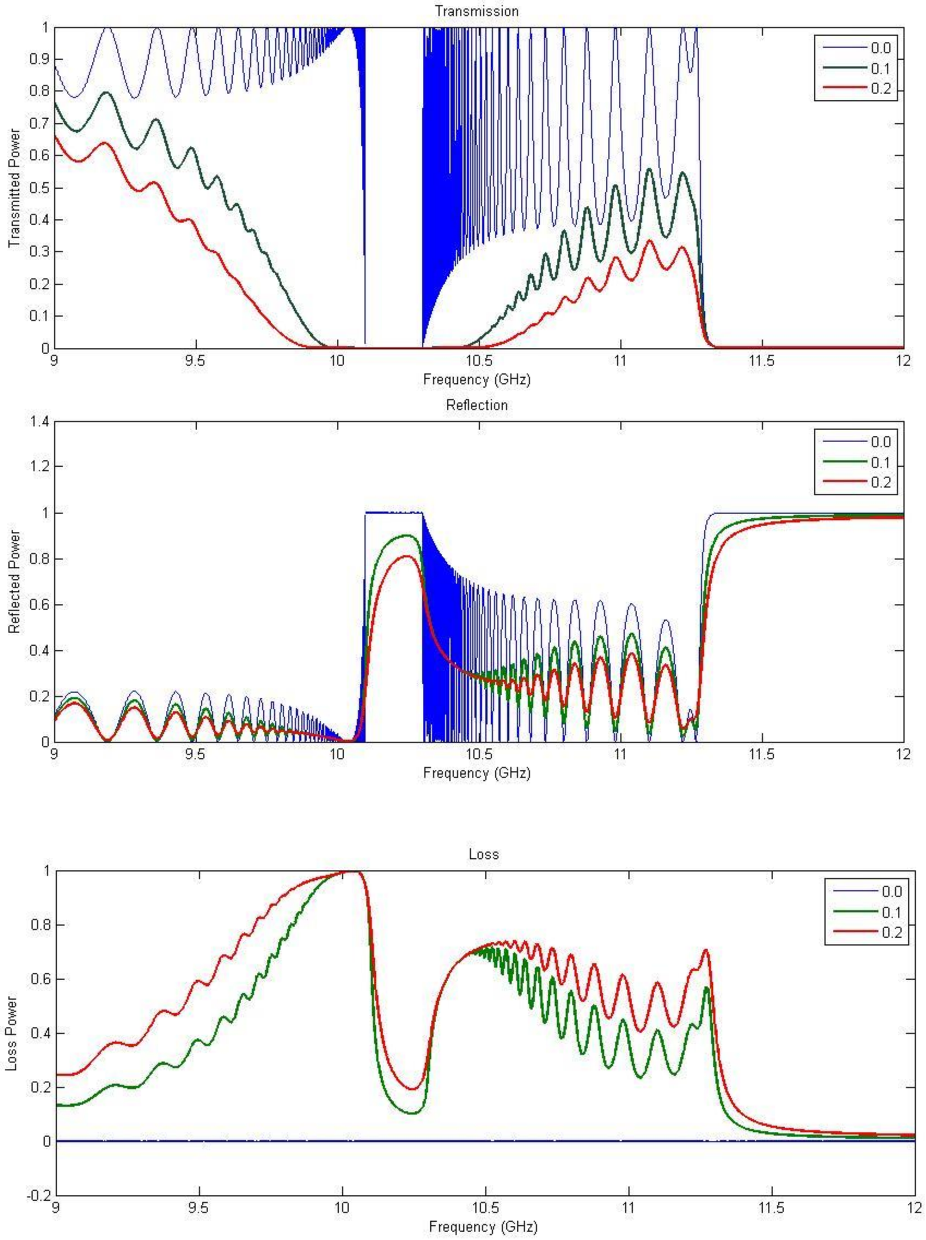

Figure (4.12): Transmitted, reflected and loss Power as a function of frequency (9-12 GHz) under the effect of various dissipation factors (γ =0.0, 0.1 and 0.2GHz). (d_{DLC} =85 nm, d_{PS} =30 nm, d_{LHM} =30 mm, n_{DLC} =1.6, n_{PS} =2.8, $\theta = 45^{\circ}$).

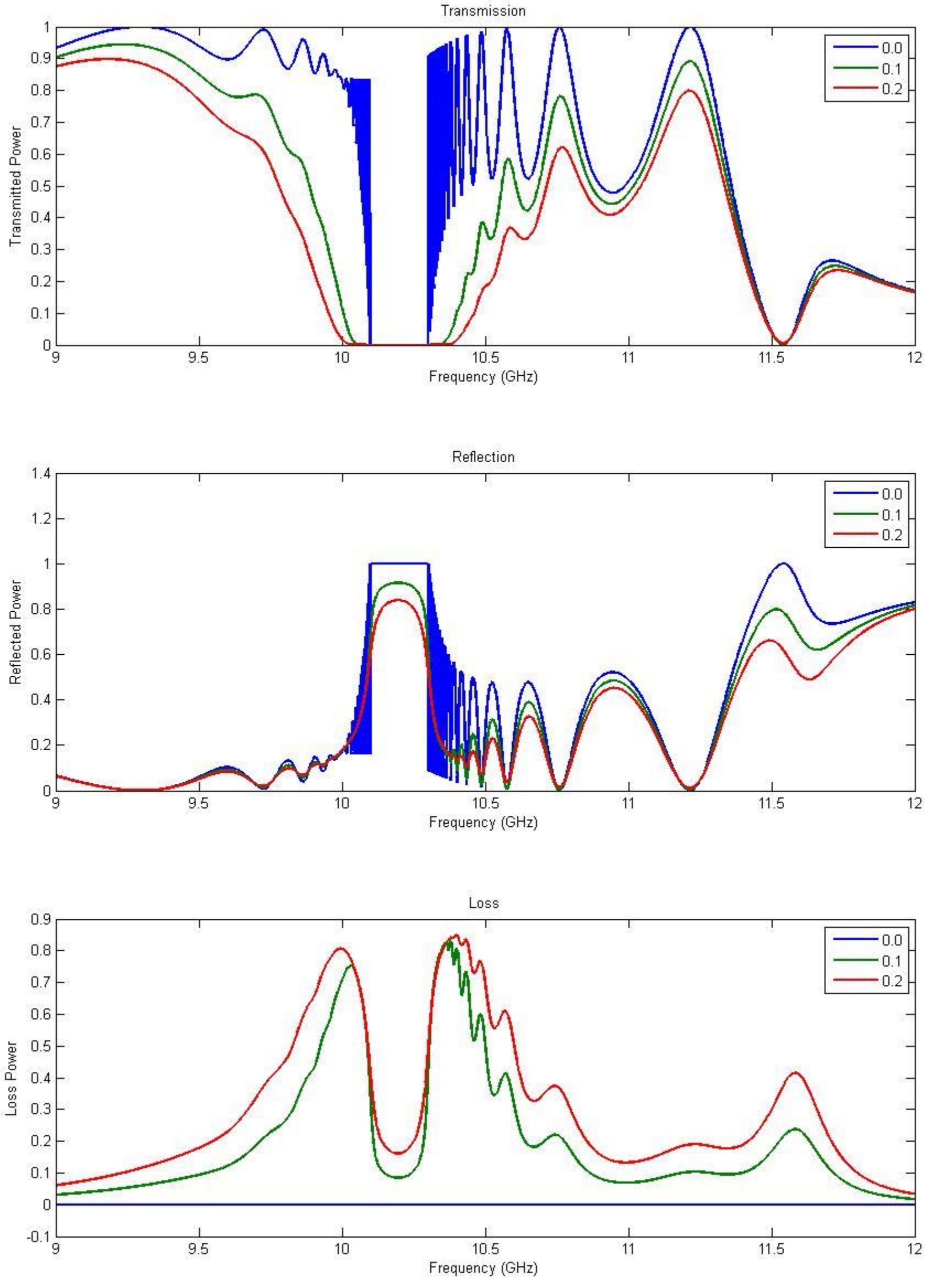

Figure (4.13): Transmitted, reflected and loss Power against frequency (9-12 GHz) under the effect of various dissipation factors (γ =0.0, 0.1and 0.2 GHz). ($d_{\text{DLC}} = d_{\text{PS}} = d_{\text{LHM}}$ =6.82 mm, n_{DLC} =1.6, n_{PS} =2.8, $\theta = 30^\circ$).

Chapter 5

Effects of Left-Handed Material on New Waveguide Structure for Solar Cell Model

5.1 Introduction

In this chapter, a transverse electric polarized (TE) waves propagation through a new waveguide structure consisting of diamond-like carbon, porous silicon and left-handed material is considered (see figure 5.1). The transfer matrix method for numerical calculation of the transmitted and reflected powers of the structure as a functions of the incident wavelength has been applied. In section 5.2, the effect of changing the angle of incidence on wave propagation through the structure has been studied. The effect of changing the value of the magnetic permeability of the left-handed component has been shown in section5.3. The values of the left-handed permeability that have been used for calculations are -4, -5, -6 and -8 as in Ref. (El-Khozondar, Al-Sahhar, & Shabat, 2010). In section 5.4, the effect of the layer thickness on wave propagation has been investigated. The effect of the composition of a waveguide structure has also been investigated in section 5.5. In section 5.6, the effect of making choices of the values of the refractive indices of the diamond-like carbon and the porous silicon has been illustrated. Miscellaneous results on the transmitted and reflected powers as a functions of incident wavelength are introduced in figure 5.2 through figure 5.15. Results of this chapter proposes the studied structure as a new waveguide model for solar cells.

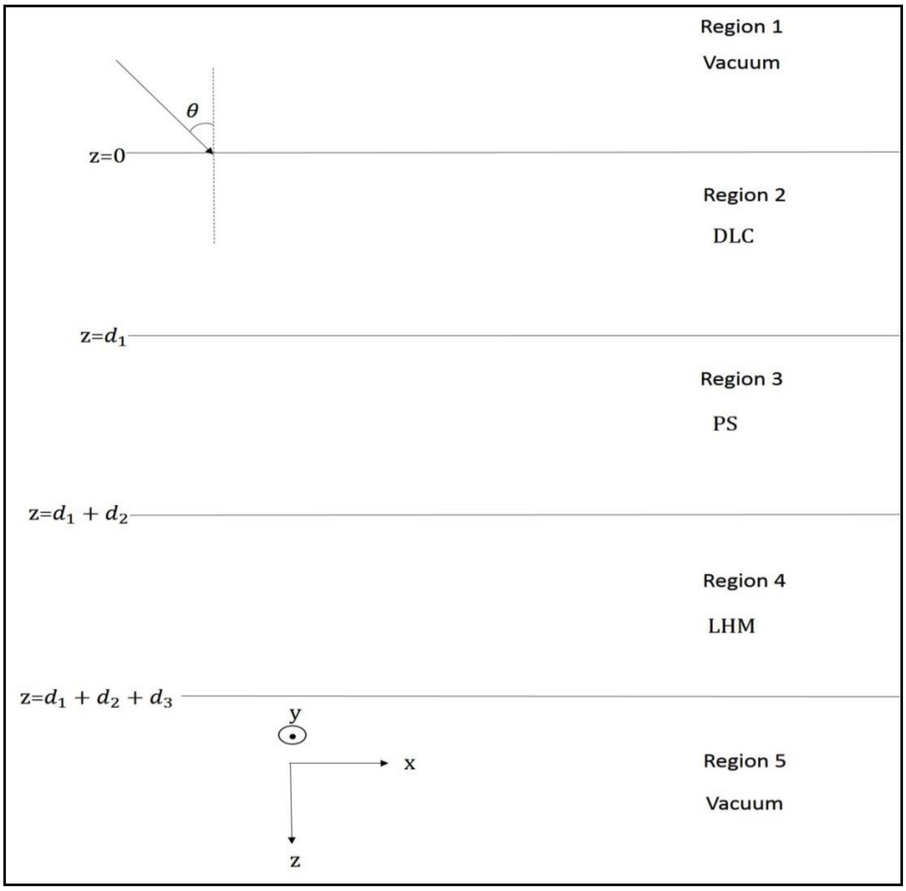

Figure (5.1): Oblique incidence of electromagnetic wave on DLC,PS and LHM structure embedded in vacuum.

5.2 Effect of the Angle of Incidence on Wave Propagation

In this section, a transverse electric waves propagate through a DLC-PS-LHM structure. The wavelength range of interest covers 400 nm to 1200 nm where a left-handed material of refractive index value -2 was found to exhibit negative refraction (Kim, Cho, Tae, & Lee, 2006). It has been shown that the behavior of the transmitted and reflected powers versus wavelength strongly depend upon the value of the permeability used.

In figure 5.2, the transmitted and reflected powers are plotted as a functions of wavelength for negative value of the LHM index of refraction (n = -2) and negative permeability ($\mu_{LHM} = -8$). The thickness of the LHM is selected to be 400 nm. As demonstrated in the figure, as theta increases, a shift to the right accompanied by broadening in the peak width is achieved. For various angles of incidence, the location of transmission peaks are different depending on the angle. The plot at 89° angle of incidence corresponds to a nulls of the transmitted powers except for certain wavelengths. In figure 5.1, the peaks get lowered and broadened as theta increases until they vanish for horizontally incident waves. In figure 5.3, we have used the same parameter as in figure 5.2 whereas the thickness of the LHM layer is reduced to 200 nm.

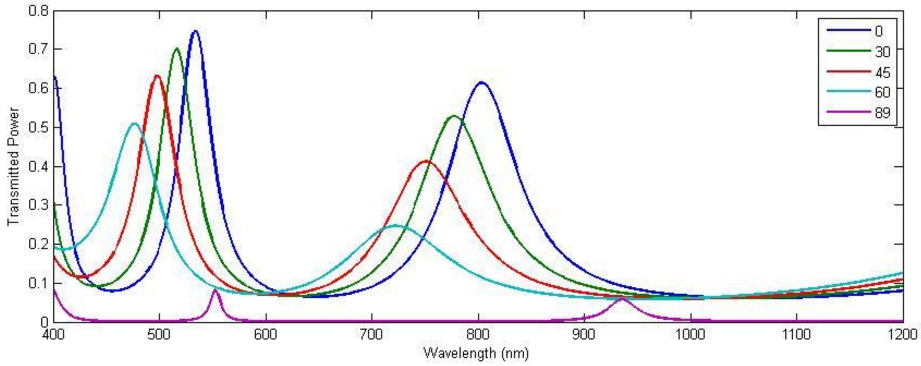

Figure (5.2): Transmitted and reflected powers as afunction of wavelength (400-1200 nm) for various angles of incidence(θ = 0˚,θ = 30˚,θ = 45˚,θ = 60˚and θ = 89˚). (d_{DLC} = 85 nm, d_{PS} = 30 nm , d_{LHM} =400 nm, n_{LHM}= -2 ,μ_{LHM} =-8, n_{DLC} =1.6, n_{PS} =2.9).

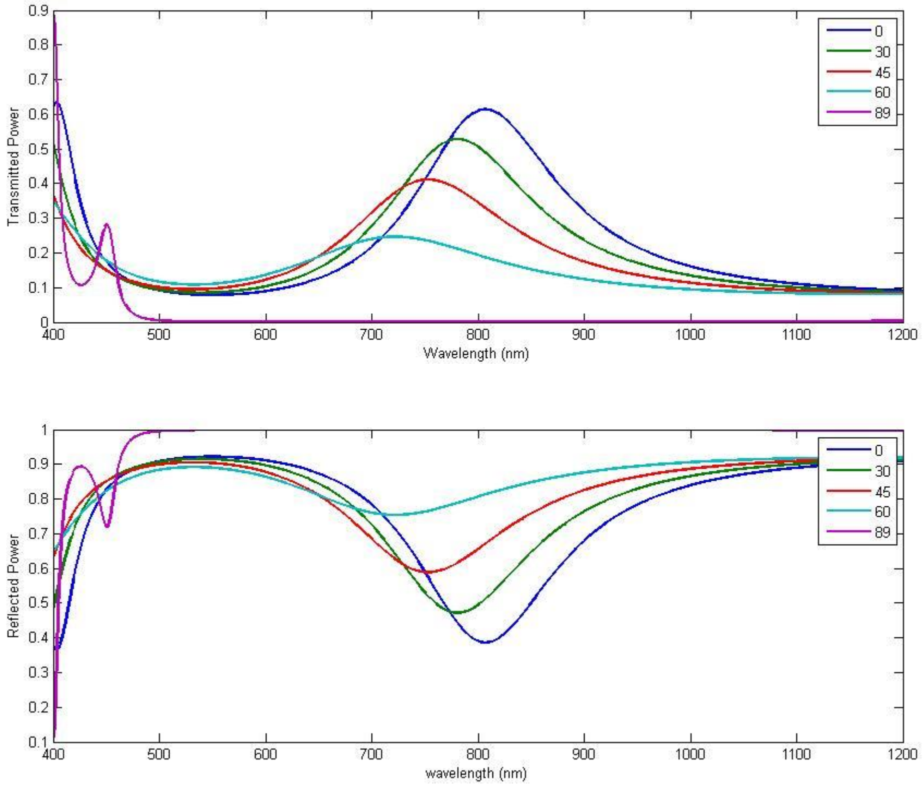

Figure (5.3): Transmitted and reflected powers as afunction of wavelength (400-1200 nm) for various angles of incidence($\theta = 0^\circ$,$\theta = 30^\circ$,$\theta = 45^\circ$,$\theta = 60^\circ$and $\theta = 89^\circ$). (d_{DLC} = 85 nm, d_{PS} = 30 nm , d_{LHM} =200 nm, n_{LHM}= -2 μ_{LHM} =-8, n_{DLC} =1.6, n_{PS} =2.9).

5.3 Effect of the Magnetic Permeability of LHM of Incidence on Wave Propagation

Figure 5.4 illustrates the transmitted and reflected powers against wavelength. For comparison purposes, we change the value of the relative permeability of the LHM. The values used for the permeability are the following: -4, -5, -6, -8. The normal incidence case (i.e., the θ= 0°) is considered. As evident in the figure, the transmitted and reflected powers depend on the magnetic permeability. For example, the value -4 results in the best transmission. At 800 nm, a value of 0.63 (0.37) for the transmitted (reflected) power is attained regardless of the value of permeability.

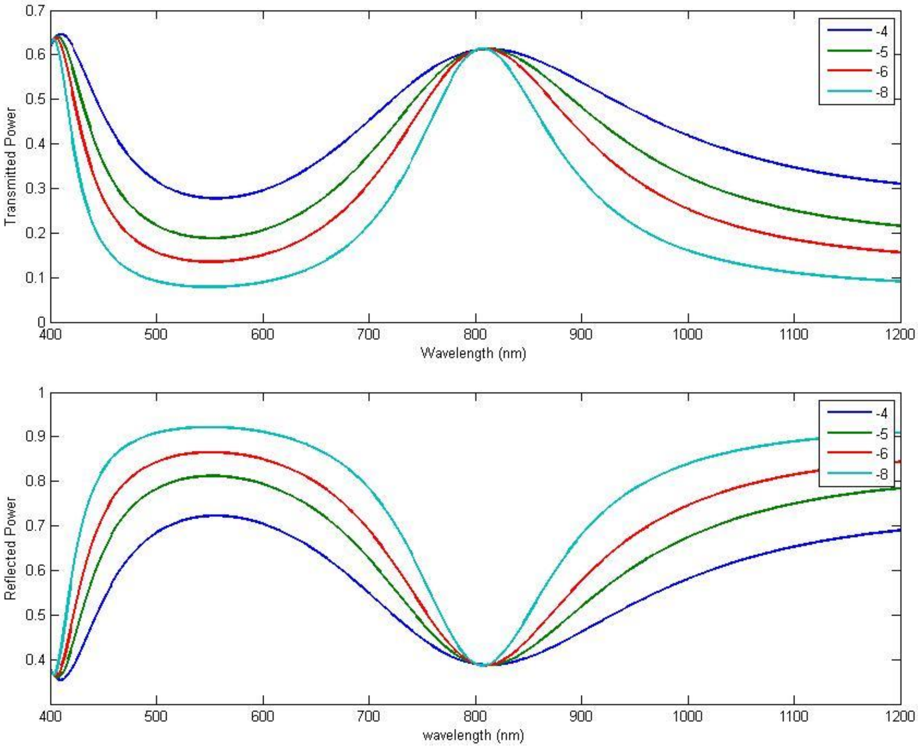

Figure (5.4): Transmitted and reflected powers as afunction of wavelength (400-1200 nm) for different values of magnetic permeability of LHM (μ_{LHM} =-4,-5,-6 and -8). (d_{DLC} = 85 nm, d_{PS} = 30 nm , d_{LHM} =200 nm, n_{LHM}= -2, n_{DLC} =1.6, n_{PS} =2.9, θ=0˚).

In figure 5.5, the transmitted and reflected powers are illustrated as a functions of wavelength as the value of the left-handed permeability changes. As evident in the figure, the higher the value of permeability the higher transmitted power is obtained. However, the effect of changing the values of permeability is ignorable at the wavelengths that lie in the vicinities of 500 nm and 750 nm. In comparison to figure 5.5, in figure (5.6), the effect of reducing the thickness of the LHM component to 200 nm on the transmitted (reflected) power can be clearly seen as the remaining parameters are kept constant.

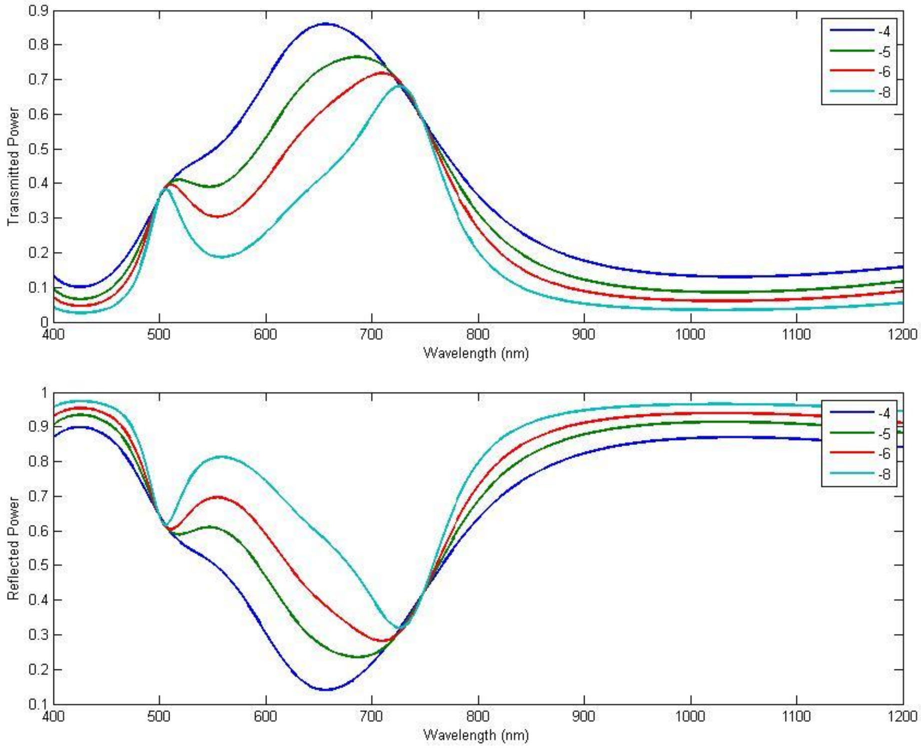

Figure (5.5): Transmitted and reflected powers as afunction of wavelength (400-1200 nm) for different values of magnetic permeability of LHM (μ_{LHM} =-4,-5,-6 and -8). (d_{DLC} = 85 nm, d_{PS} = 30 nm , d_{LHM} =400 nm, n_{LHM}= -2, n_{DLC} =2.7, n_{PS} =3, θ = 45˚).

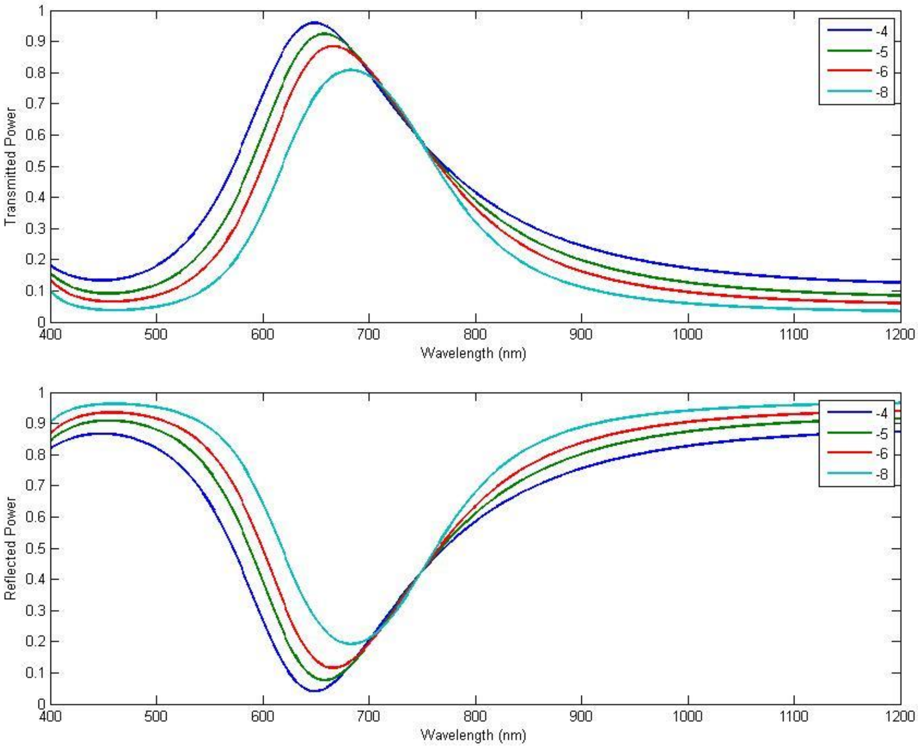

Figure (5.6): Transmitted and reflected powers as afunction of wavelength (400-1200 nm) for different values of magnetic permeability of LHM (μ_{LHM} =-4,-5,-6 and -8). (d_{DLC} = 85 nm, d_{PS} = 30 nm , d_{LHM} =200 nm, n_{LHM}= -2, n_{DLC} =2.7, n_{PS} =3, θ = 45˚).

5.4 Effect of Changing the Thickness on Wave Propagation

In figure 5.7, the effect of changing the thickness of the left-handed material in the structure is shown. As confirmed from the figure, the plots would be slightly differentiated from one another when the thickness varies and they reach a maximum of the transmitted power (~1) at 630 nm.

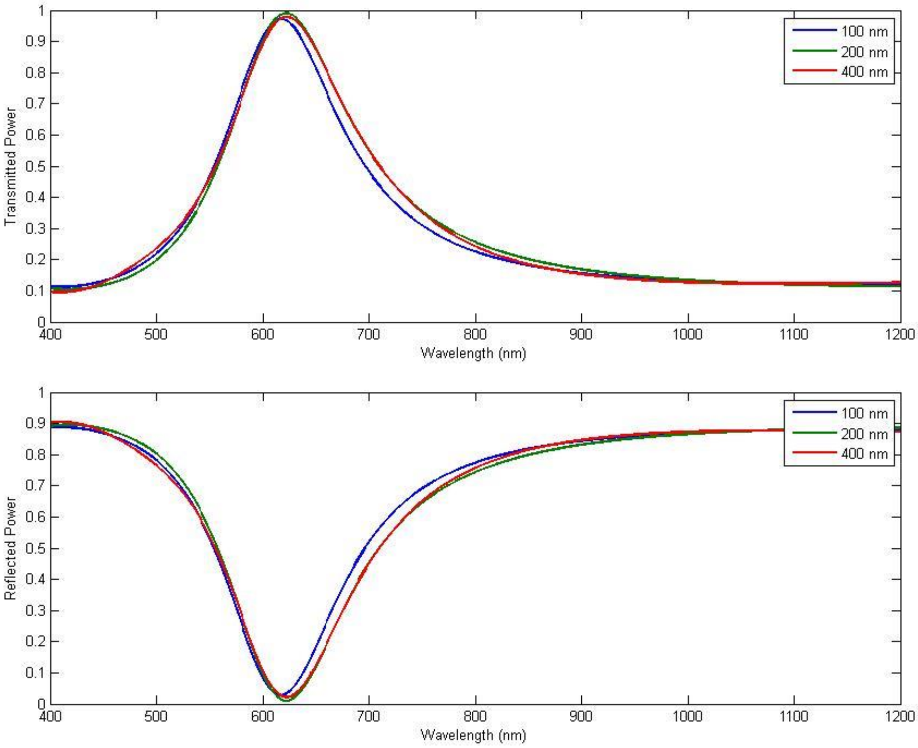

Figure (5.7): Transmitted and reflected powers as afunction of wavelength (400-1200 nm) for different thicknesses of LHM: d_{LHM} =100, 200 and 400 nm. (d_{DLC} = 85 nm, d_{PS} = 30 nm , n_{LHM}= -2, μ_{LHM} =-4, n_{DLC} =2.7, n_{PS} =3, $\theta = 60^{\circ}$).

In figure 5.8, for comparison, two thicknesses of LHM (200 nm and 400 nm) have been tried for the permeability value (-4) that optimizes the transmitted power as evident in previous figures. The normal incidence case ($\theta = 0^{\circ}$) is considered. As seen in figure 5.8, the 200 nm thickness results in a higher transmission than that of the other for the entire wavelength range except for the wavelength interval (480-600 nm) where a prominent peak does exist.

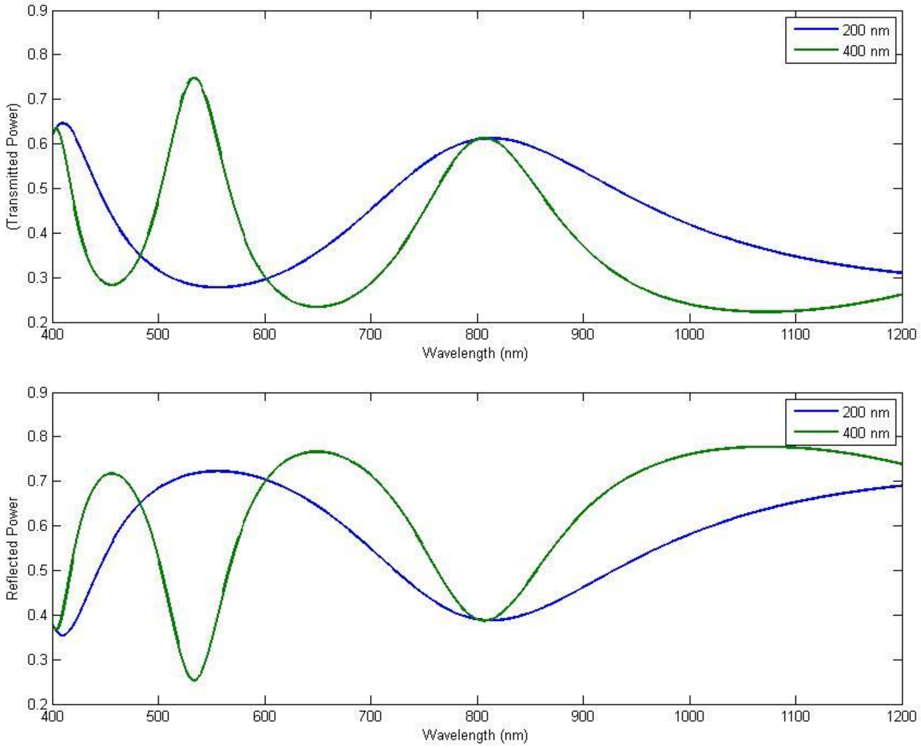

Figure (5.8): Transmitted and reflected powers as a function of wavelength (400-1200 nm) for two different thicknesses of LHM: d_{LHM} =200 nm and d_{LHM} =400 nm. (d_{DLC} = 85 nm, d_{PS} = 30 nm , n_{LHM}= -2, μ_{LHM} =-4, n_{DLC} =1.6, n_{PS} =2.9, $\theta = 0^{\circ}$).

For comparison, figure 5.9 illustrates the transmitted and reflected powers versus the incident wavelength for two different cases of thickness:

Case 1: (d_{DLC}=85 nm, d_{PS}= 30 nm).

Case 2: (d_{DLC}=86.9 nm, d_{PS}= 47.9 nm).

In either case, the thickness of LHM is 200 nm, the refractive index of LHM is –2 and the permeability is -4. The normal incidence case is considered. As seen in the figure (5.9), the plot that corresponds to the second case portrayed as a blue shift of that of the first case in the range (740 - 1200 nm) and as a red shift in the range (400 – 740 nm).

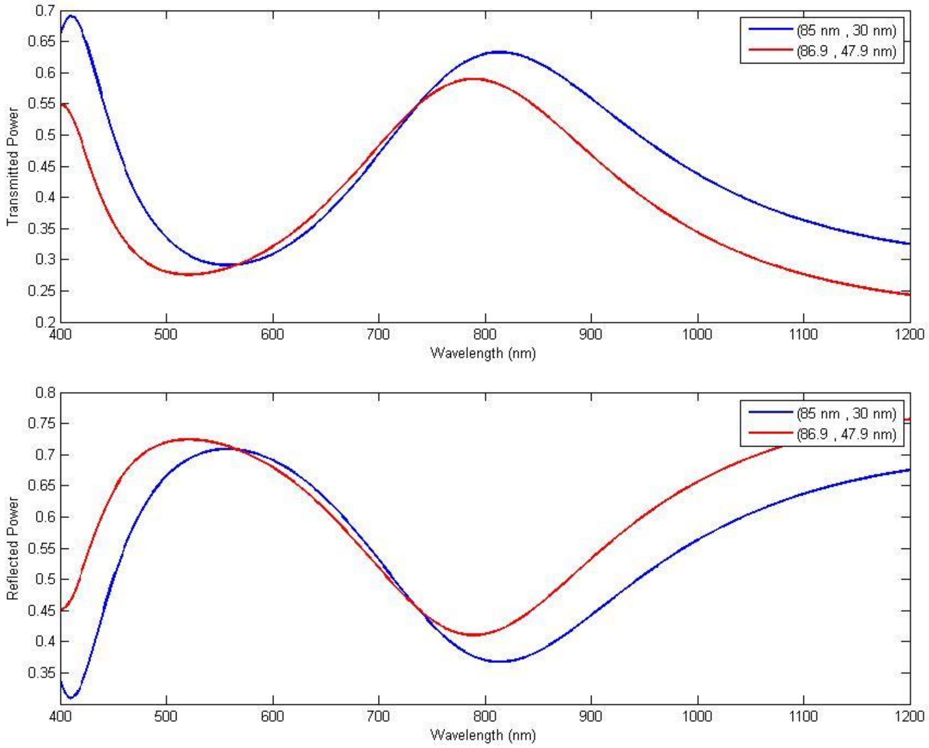

Figure (5.9): Transmitted and reflected powers as afunction of wavelength (400-1200 nm) under the effect of changing the refractive idecies and thicknesses of DLC and PS. (d_{DLC} = 85 nm/86.9 nm, d_{PS} = 30 nm/47.9 nm, d_{LHM} =200 nm, n_{LHM}= -2, μ_{LHM} =-4, n_{DLC} =1.6, n_{PS} =2.8, $\theta = 0^{\circ}$).

In figure 5.10, the transmitted and reflected powers are plotted as a functions of wavelength for different thicknesses of left-handed layer, namely, 0 nm, 200 nm, 300 nm, 400 nm and 500 nm. Unlike the other plots, the zero thickness- plot exhibits the highest transmission (0.6 - 0.75) along the entire wavelength range. In addition, a conspicuous feature is that this plot is crossed by the others at certain wavelengths.

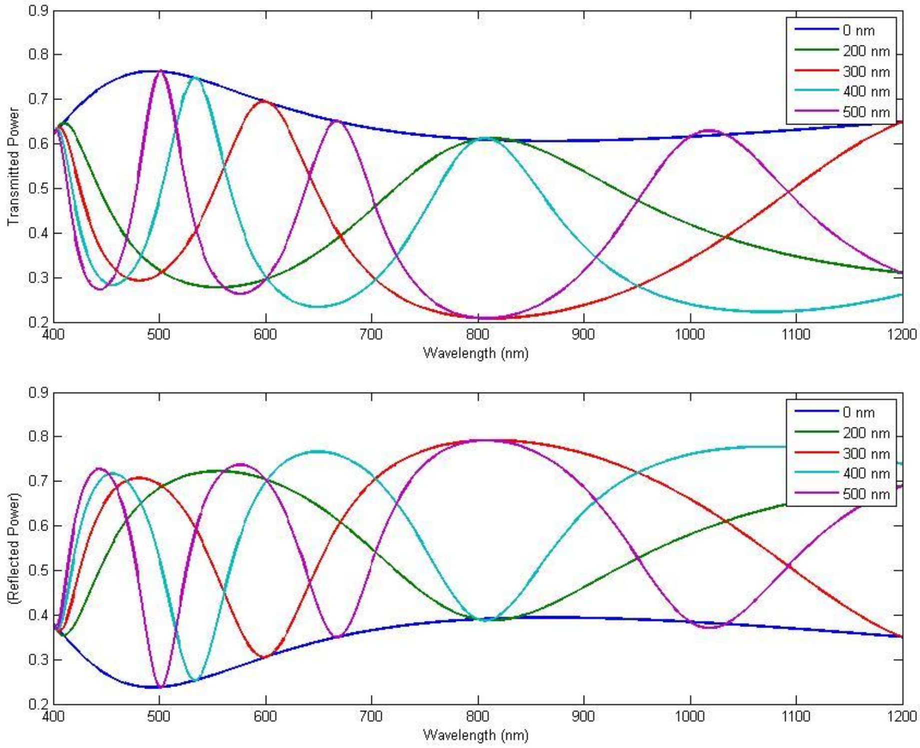

Figure (5.10): Transmitted and reflected powers as afunction of wavelength (400-1200 nm) for various thicknesses of LHM: (d_{LHM} =0, 200, 300, 400 and 500 nm). (d_{DLC} = 85 nm, d_{PS} = 30 nm , n_{LHM}= -2, μ_{LHM} =-4, n_{DLC} =1.6, n_{PS} =2.9, θ = 0˚).

5.5 Effect of the Composition of the Waveguide Structure on Wave Propagation

In figure 5.11, the transmitted and reflected powers are portrayed as a functions of wavelength while changing the structures composition. As evident in the figure, among the three different structures, the LHM single layer exhibits the best results for the transmitted and reflected powers in the wavelength range (600-1200 nm). However, this is no longer the best for the wavelengths (400-600 nm) since the DLC/PS doublelayer works better in this range. However, the DLC/PS/LHM structure exhibits higher transmission than that of the LHM as a single layer in the range (500-600 nm) and also than that of the DLC/PS doublelayer in the range (600-800 nm). As seen for the red plot, the transmitted power attains a maximum of 0.8. In figure 5.12, by comparing the three sorts of structure for the wavelength intervals (460-520 nm) and (700-800 nm), the choice of the DLC/PS/LHM structure results in an improved transmitted power.

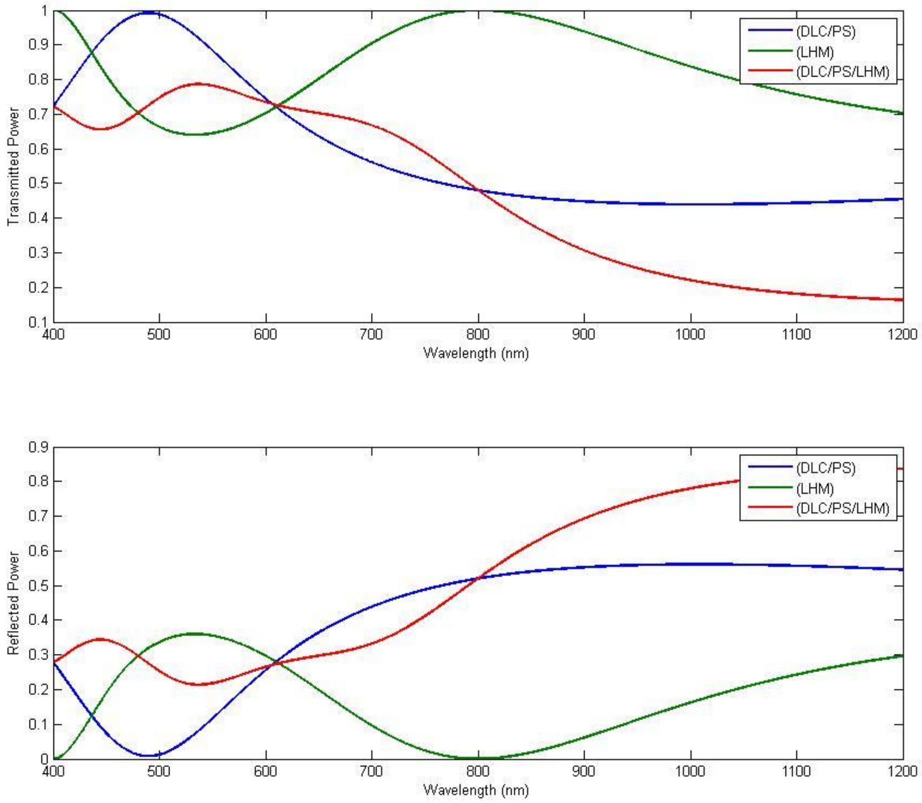

Figure (5.11): Transmitted and reflected powers as afunction of wavelength (400-1200 nm) for different types of structure (DLC/PS double layer, LHM single layer and DLC/PS/LHM trilayer). (d_{DLC} = 85.9 nm, d_{PS} = 47.9 nm , d_{LHM} =200 nm, n_{LHM}= -2, μ_{LHM} =-4, n_{DLC} =2.7, n_{PS} =1.25, $\theta = 0^\circ$).

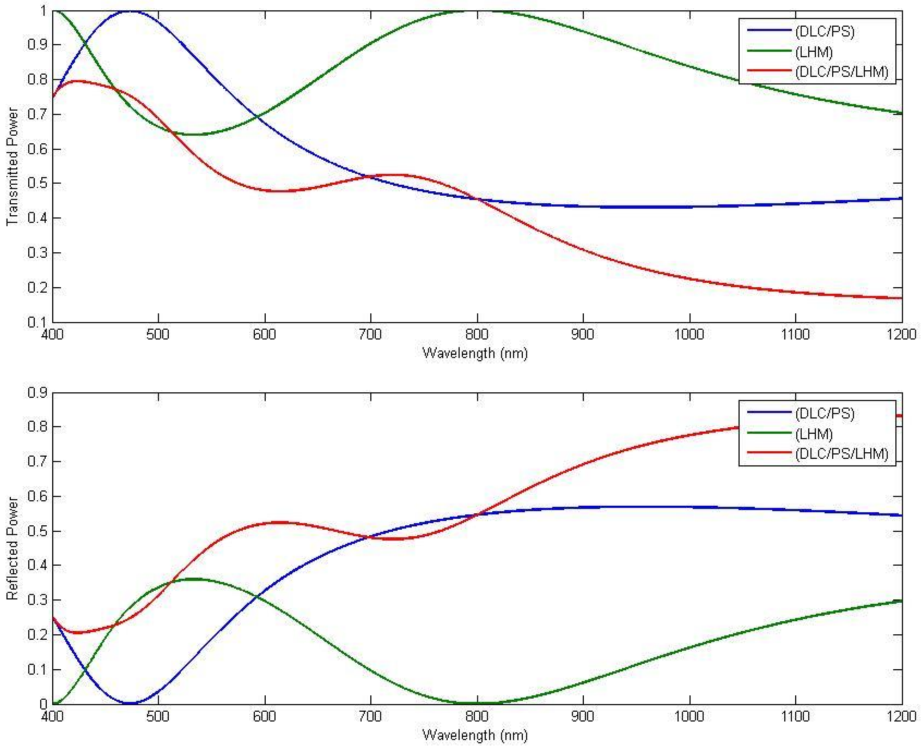

Figure (5.12): Transmitted and reflected powers as afunction of wavelength (400-1200 nm) for different types of structure (DLC/PS double layer, LHM single layer and DLC/PS/LHM trilayer). (d_{DLC} = 85 nm, d_{PS} = 30 nm , d_{LHM} =200 nm, n_{LHM}= -2, μ_{LHM} =-4, n_{DLC} =2.7, n_{PS} =1.25, $\theta = 0^{\circ}$).

In figure 5.13, the green plot shows transmitted power ranges from 0.72 to 1 along the entire wavelength range. Also, the blue plot shows a relatively high transmission compared to the red at most wavelengths. However, a little improvement in the transmitted power (~ 0.8) is obtained for the red plot around 510 nm.

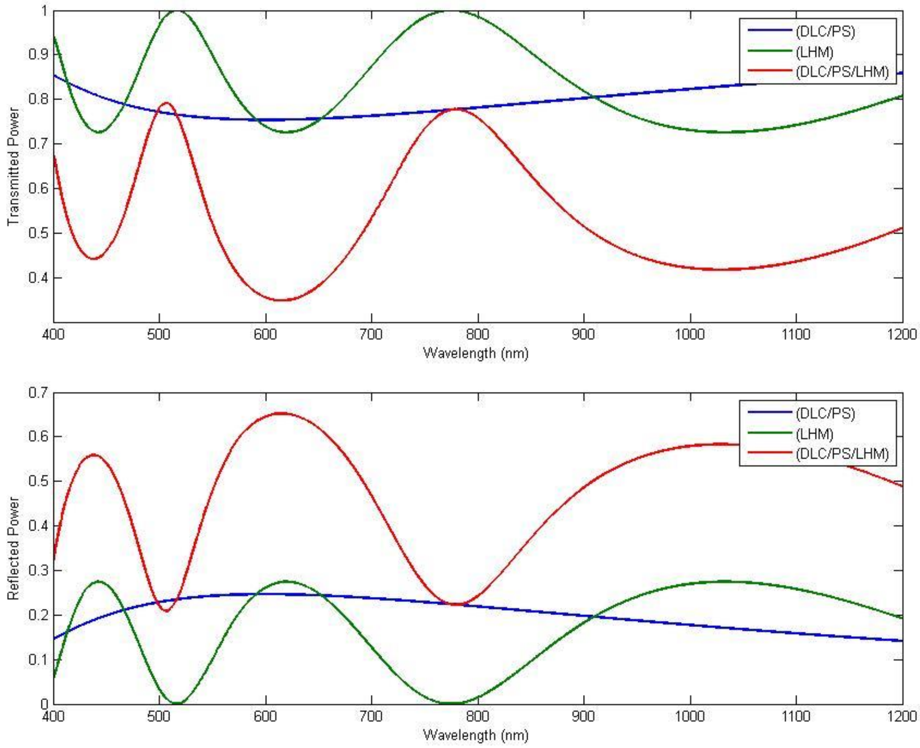

Figure (5.13): Transmitted and reflected powers as afunction of wavelength (400-1200 nm) for different types of structure (DLC/PS double layer, LHM single layer and DLC/PS/LHM trilayer). (d_{DLC} = 85 nm, d_{PS} = 30 nm , d_{LHM} =400 nm, n_{LHM}= -2, μ_{LHM} =-4, n_{DLC} =1.6, n_{PS} =1.25, $\theta = 30^{\circ}$).

5.6 Effect of Changing the Value of the Refractive Index of Diamond-Like Carbon and Porous Silicon on Wave Propagation

In figure 5.14, the transmitted and reflected powers are plotted versus wavelength for the normal incidence case in order to study the effect of making choices of the values of the refractive indices of the DLC and the PS for the case $\mu_{LHM} = -4$. As shown in the figure, by changing the values of refractive indices, a high transmitted power (~ 0.9) for some wavelength intervals has been obtained.

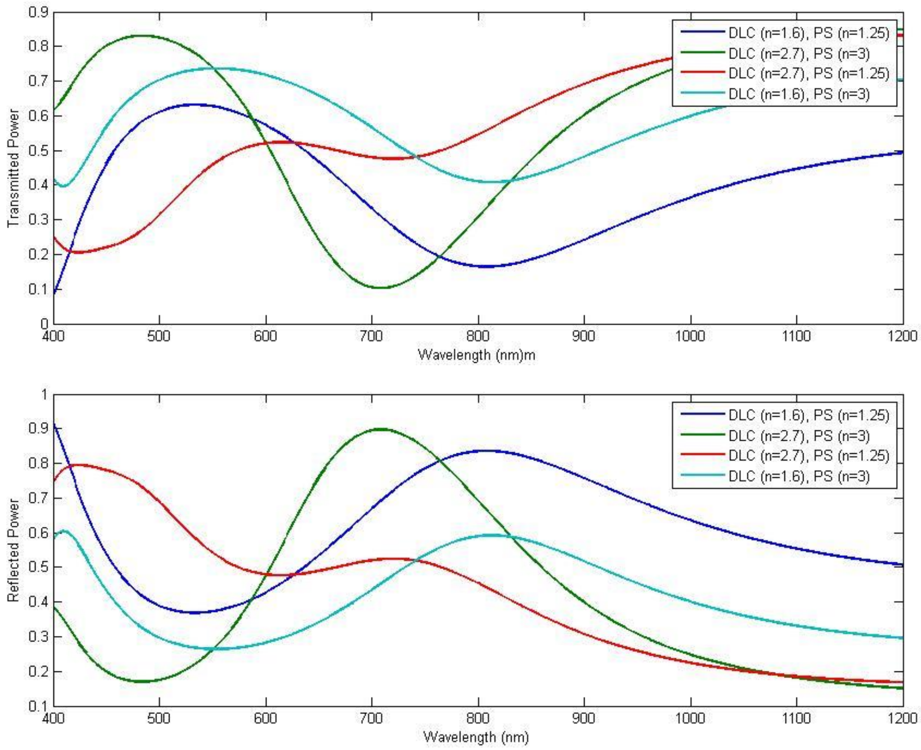

Figure (5.14): Transmitted and reflected powers as afunction of wavelength (400-1200 nm) for different values of refractive indcies of DLC and PS: (d_{DLC} = 85 nm, d_{PS} = 30 nm , d_{LHM} =200 nm, n_{LHM}= -2, μ_{LHM} =-4, θ = 0˚).

Compared to figure 5.14, figure 5.15 illustrates the transmitted and reflected powers while changing the values of the refractive indices of DLC and PS for 60° angle of incidence. As shown in the figure, the green and red plots represents totally transmitted waves at 450 and 630 nanometer wavelengths.

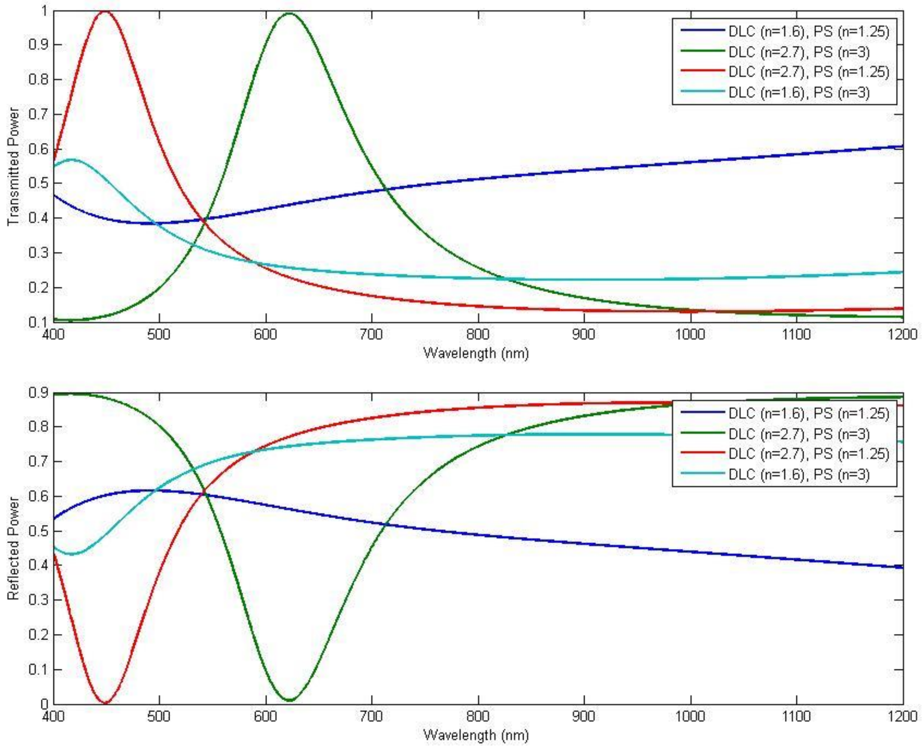

Figure (5.15): Transmitted and reflected powers as afunction of wavelength (400-1200 nm) for different values of refractive indcies of DLC and PS: (d_{DLC} = 85 nm, d_{PS} = 30 nm , d_{LHM} =200 nm, n_{LHM}= -2, μ_{LHM} =-4, $\theta = 60^\circ$).

Conclusion

This thesis aimed to numerical and analytical investigations of the electromagnetic wave propagation through a new multilayered structure consisting of diamond-like carbon, porous silicon and left-handed material. Indeed, we were interested in the porous silicon and the diamond-like carbon to be a part of this study because of their physical, mechanical and tribological properties that effectively contribute to the field of solar cells. Also, the left-handed materials are phenomenal due to the property of negative refraction and backward propagation.

A mathematical and numerical analysis for the propagation of a transverse-electric (TE) plane polarized wave incident on the structure have been carried out using the transfer matrix approach in order to compute the transmitted, reflected powers. The characteristic matrix that relates the electromagnetic fields at the first and last boundaries of the whole structure has been theoretically derived in order to formulate the transmitted and reflected powers. The transmitted and reflected powers of a structure consisting of diamond-like carbon porous silicon and left-handed material have been plotted versus the wavelength range (400-1200 nm). The effects of varying parameters such as the angle of incidence, magnetic permeability of LHM, thickness and refractive index have been studied. As confirmed from figures 5.11 and 5.12, for specific intervals of wavelength, the transmitted power of each of the left-handed layer and DLC/PS double layer was improved by adding one to another.

In general, results of this study showed that a high transmission of an incoming electromagnetic waves in the wavelength range (400-1200 nm) can be achieved. Based on these results, our proposed (DLC-PS-LHM) structure would serve as a new protective anti-reflecting coating model for solar cells since it has the advantage of lowering the surface reflections.

References

Adamian, Z., Hakhoyan, A., Aroutiounian, V., Barseghian, R., & Touryan, K. (2000). Investigations of solar cells with porous silicon as antireflection layer. *Solar energy materials and solar cells, 64*(4), 347-351.

Antipov, S. P., W. Liu, et al. (2005). Left-handed metamaterials studies and their application to accelerator physics. Particle Accelerator Conference.IEEE.

Aouida, S., Saadoun, M., Boujmil, M., Rabha, M. B., & Bessaıs, B. (2004). Effect of UV irradiations on the structural and optical features of porous silicon: application in silicon solar cells. *Applied Surface Science, 238*(1), 193-198.

Aroutiounian, V., Martirosyan, K., & Soukiassian, P. (2004). Low reflectance of diamond-like carbon/porous silicon double layer antireflection coating for silicon solar cells. *Journal of Physics D: Applied Physics, 37*(19), L25.

Aziz, W. J., Ramizy, A., Ibrahim, K., Hassan, Z., & Omar, K. (2011). The effect of anti-reflection coating of porous silicon on solar cells efficiency. *Optik-International Journal for Light and Electron Optics, 122*(16), 1462-1465.

Bilyalov, R., Lüdemann, R., Wettling, W., Stalmans, L., Poortmans, J., Nijs, J., et al. (2000). Multicrystalline silicon solar cells with porous silicon emitter. *Solar energy materials and solar cells, 60*(4), 391-420.

Bilyalov, R., Stalmans, L., Beaucarne, G., Loo, R., Caymax, M., Poortmans, J., et al. (2001). Porous silicon as an intermediate layer for thin-film solar cell. *Solar energy materials and solar cells, 65*(1), 477-485.

Bisi, O., S. Ossicini, et al. (2000). "Porous silicon: a quantum sponge structure for silicon based optoelectronics." Surface science reports 38(1): 1-126

Butt, M., Khaleeq-ur-Rahman, M., Ali, D., Akmal, A., & Naseem, S. (2015). Deposition and characterization of multilayer DLC: Mo thin films grown on silicon substrate by off-axis pulsed laser deposition technique. *Applied Surface Science, 331*, 407-414.

Chen, L., Yang, M., Song, C., Yu, B., & Qian, L. (2013). Is 2nm DLC coating enough to resist the nanowear of silicon. *Wear, 302*(1), 909-917.

El-Khozondar, H. J., Al-Sahhar, Z. I., & Shabat, M. M. (2010). Electromagnetic surface waves of a ferrite slab bounded by metamaterials. *AEU-International Journal of Electronics and Communications, 64*(11), 1063-1067.

González-Díaz, B., Guerrero-Lemus, R., Borchert, D., Hernández-Rodríguez, C., & Martínez-Duart, J. (2007). Low-porosity porous silicon nanostructures on monocrystalline silicon solar cells. *Physica E: Low-dimensional Systems and Nanostructures, 38*(1), 215-218.

Hatada, R., Flege, S., Bobrich, A., Ensinger, W., & Baba, K. (2014). Surface modification and corrosion properties of implanted and DLC coated stainless steel by plasma based ion implantation and deposition. *Surface and Coatings Technology, 256*, 23-29.

Ikeyama, M., & Sonoda, T. (2013). Transparent Si–DLC coatings on metals with high repetition bi-polar pulses of a PBII system. *Nuclear Instruments and Methods in Physics Research Section B: Beam Interactions with Materials and Atoms, 307*, 340-343.

Kafesaki, M., Koschny, T., Zhou, J., Katsarakis, N., Tsiapa, I., Economou, E., et al. (2007). Electromagnetic behaviour of left-handed materials. *Physica B: Condensed Matter*, *394*(2), 148-154.

Kalin, M., Kogovšek, J., & Remškar, M. (2013). Nanoparticles as novel lubricating additives in a green, physically based lubrication technology for DLC coatings. *Wear, 303*(1), 480-485.

Kim, K. Y., Cho, Y. K., Tae, H.-S., & Lee, J. (2006). Guided mode propagations of grounded double-positive and double-negative metamaterial slabs with arbitrary material indexes. *JOURNAL-KOREAN PHYSICAL SOCIETY, 49*(2), 577.

Klyui, N., V. Litovchenko, et al. (2002). "Silicon solar cells with antireflection diamond-like carbon and silicon carbide films." Solar energy materials and solar cells 72(1): 597-603.

Litovchenko, V., & Klyui, N. (2001). Solar cells based on DLC film–Si structures for space application. *Solar energy materials and solar cells, 68*(1), 55-70.

Liu, Y., & Zhang, X. (2011). Metamaterials: a new frontier of science and technology. *Chemical Society Reviews, 40*(5), 2494-2507.

Masuko, M., Ono, T., Aoki, S., Suzuki, A., & Ito, H. (2015). Friction and wear characteristics of DLC coatings with different hydrogen content lubricated with several Mo-containing compounds and their related compounds. *Tribology International, 82*, 350-357.

Mobarak, H., & Chowdhury, M. (2014). Tribological Performance of Hydrogenated Amorphous Carbon (aC: H) DLC Coating when Lubricated with Biodegradable Vegetal Canola Oil. *Tribology in Industry, 36*(2).

Mutafov, P., Lanigan, J., Neville, A., Cavaleiro, A., & Polcar, T. (2014). DLC-W coatings tested in combustion engine—Frictional and wear analysis. *Surface and Coatings Technology, 260*, 284-289.

Okubo, H., Tsuboi, R., & Sasaki, S. (2015). Frictional properties of DLC films in low-pressure hydrogen conditions. *Wear, 340*, 2-8.

Pandey, G., Kumar, A., & Thapa, K. B. (2013). Frequency Dependence Effective Refractive Index of Meta–Materials by Effective Medium Theory.ISSN, Vo.(3), 2231-1297.

Park, K., Lee, B. J., Fu, C., & Zhang, Z. M. (2005). Study of the surface and bulk polaritons with a negative index metamaterial. *JOSA B, 22*(5), 1016-1023.

Pasakawee, S. (2012). Left-handed metamaterials realized by complementary split-ring resonators for RF and microwave circuit applications.

Pendry, J. B., Holden, A. J., Robbins, D., & Stewart, W. (1999). Magnetism from conductors and enhanced nonlinear phenomena. *Microwave Theory and Techniques, IEEE Transactions on, 47*(11), 2075-2084.

Rabha, M. B., & Bessaïs, B. (2010). Enhancement of photovoltaic properties of multicrystalline silicon solar cells by combination of buried metallic contacts and thin porous silicon. *Solar Energy, 84*(3), 486-491.

Ramachandran, S., Tao, L., Lee, T., Sant, S., Overzet, L., Goeckner, M., et al. (2006). Deposition and patterning of diamondlike carbon as antiwear nanoimprint templates. *Journal of Vacuum Science & Technology B, 24*(6), 2993-2997.

Ramakrishna, S. A. (2005). Physics of negative refractive index materials. *Reports on Progress in Physics, 68*(2), 449.

Ramizy, A., Aziz, W. J., Hassan, Z., Omar, K., & Ibrahim, K. (2011). Improved performance of solar cell based on porous silicon surfaces. *Optik-International Journal for Light and Electron Optics, 122*(23), 2075-2077.

Ramizy, A., Hassan, Z., Omar, K., Al-Douri, Y., & Mahdi, M. (2011). New optical features to enhance solar cell performance based on porous silicon surfaces. *Applied Surface Science, 257*(14), 6112-6117.

Ran, L.-X., Huang-Fu, J. T., Chen, H., Zhang, X.-M., Chen, K. S., Grzegorczyk, T. M., et al. (2005). Experimental study on several left-handed matamaterials. *Progress In Electromagnetics Research, 51*, 249-279.

Saadoun, M., Ezzaouia, H., Bessaıs, B., Boujmil, M., & Bennaceur, R. (1999). Formation of porous silicon for large-area silicon solar cells: a new method. *Solar energy materials and solar cells, 59*(4), 377-385.

Salman, K. A., Omar, K., & Hassan, Z. (2012). *Effect of etching time on porous silicon processing.* Paper presented at the INTERNATIONAL CONFERENCE ON NANOTECHNOLOGY-RESEARCH AND COMMERCIALIZATION 2011:(ICONT 2011).

Seker, Z., Ozdamar, H., Esen, M., Esen, R., & Kavak, H. (2014). The effect of nitrogen incorporation in DLC films deposited by ECR Microwave Plasma CVD. *Applied Surface Science, 314,* 46-51.

Shabat, M. M., Ubeid, M. F., & Sid-Ahmed, M. O. (2014). *Calculation of reflected and transmitted powers of a metamaterial waveguide structure using MAPLE software.* Paper presented at the 12th Education and Training in Optics and Photonics Conference.

Sharma, R., Barhai, P., & Kumari, N. (2008). Corrosion resistant behaviour of DLC films. *Thin Solid Films, 516*(16), 5397-5403.

Smith, D. R., Padilla, W. J., Vier, D., Nemat-Nasser, S. C., & Schultz, S. (2000). Composite medium with simultaneously negative permeability and permittivity. *Physical review letters, 84*(18), 4184.

Soukoulis, C. M., Kafesaki, M., & Economou, E. N. (2006). Negative-Index Materials: New Frontiers in Optics. *Advanced materials, 18*(15), 1941-1952.

Staia, M., Cabrera, E. P., Iost, A., Zairi, A., Belayer, S., & Van Gorp, A. (2015). Tribological response of AA 2024-T3 aluminium alloy coated with a DLC duplex coating. *Tribology International, 85,* 74-87.

Tasdemir, H. A. (2014). *Boundary Lubrication Mechanisms of Diamond-Like Carbon Coatings with Oil Additives.* NAGOYA UNIVERSITY.

Ubeid, M. F., Shabat, M. M., & Sid-Ahmed, M. O. (2013) (PhD). Reflection and transmission of electromgantic waves by a layered structure containing Left-handed Material, Sudan University of Science and Technology, Sudan.

Ubeid, M. F., Shabat, M. M., & Sid-Ahmed, M. O.(2012). Effect of damping coefficient of precession on the transmission of electromagnetic waves through a structure containing ferromagnetic material waveguide.

Ubeid, M. F., Shabat, M. M., & Sid-Ahmed, M. O. (2012). Numerical study of negative-refractive index ferrite waveguide. *Journal of Nano-and Electronic Physics, 4*(1), 1009-1001.

Veselago, V., Braginsky, L., Shklover, V., & Hafner, C. (2006). Negative refractive index materials. *Journal of Computational and Theoretical Nanoscience, 3*(2), 189-218.

Vetter, J. (2014). 60years of DLC coatings: Historical highlights and technical review of cathodic arc processes to synthesize various DLC types, and their evolution for industrial applications. *Surface and Coatings Technology, 257,* 213-240.

Vitanov, P., Delibasheva, M., Goranova, E., & Peneva, M. (2000). The influence of porous silicon coating on silicon solar cells with different emitter thicknesses. *Solar energy materials and solar cells, 61*(3), 213-221.

Vitanov, P., Goranova, E., Stavrov, V., Ivanov, P., & Singh, P. (2009). Fabrication of buried contact silicon solar cells using porous silicon. *Solar energy materials and solar cells, 93*(3), 297-300.

Vitu, T., Escudeiro, A., Polcar, T., & Cavaleiro, A. (2014). Sliding properties of Zr-DLC coatings: The effect of tribolayer formation. *Surface and Coatings Technology, 258,* 734-745.

Widom, A., & Drosdoff, D. (2005). Snell's law from an elementary particle viewpoint. *American journal of physics*(10), 973-975.

Yan, C., Wang, Q., & Cui, Y. (2010). Generating mechanism of the energy-stream loops for the evanescent waves in a left-handed material slab. *Optik-International Journal for Light and Electron Optics*, *121*(1), 63-67.

Yan, X., Xu, T., Yang, S., Liu, H., & Xue, Q. (2004). Characterization of hydrogenated diamond-like carbon films electrochemically deposited on a silicon substrate. *Journal of Physics D: Applied Physics*, *37*(17), 2416.

Yang, W., Guo, Y., Xu, D., Li, J., Wang, P., Ke, P., et al. (2015). Microstructure and properties of (Cr: N)-DLC films deposited by a hybrid beam technique. *Surface and Coatings Technology, 261*, 398-403.

Zhang, X. (2004). Absolute negative refraction and imaging of unpolarized electromagnetic waves by two-dimensional photonic crystals. *Physical Review B*, *70*(20), 205102.